Sustained eruptions on Enceladus explained by turbulent dissipation in tiger stripes

Edwin S. Kite[a,1] and Allan M. Rubin[b]

[a]Department of Geophysical Sciences, University of Chicago, Chicago, IL 60637; and [b]Department of Geosciences, Princeton University, Princeton, NJ 08544

Spacecraft observations suggest that the plumes of Saturn's moon Enceladus draw water from a subsurface ocean, but the sustainability of conduits linking ocean and surface is not understood. Observations show eruptions from "tiger stripe" fissures that are sustained (although tidally modulated) throughout each orbit, and since the 2005 discovery of the plumes. Peak plume flux lags peak tidal extension by ∼1 rad, suggestive of resonance. Here, we show that a model of the tiger stripes as tidally flexed slots that puncture the ice shell can simultaneously explain the persistence of the eruptions through the tidal cycle, the phase lag, and the total power output of the tiger stripe terrain, while suggesting that eruptions are maintained over geological timescales. The delay associated with flushing and refilling of $O(1)$-m-wide slots with ocean water causes erupted flux to lag tidal forcing and helps to buttress slots against closure, while tidally pumped in-slot flow leads to heating and mechanical disruption that staves off slot freezeout. Much narrower and much wider slots cannot be sustained. In the presence of long-lived slots, the 10^6-y average power output of the tiger stripes is buffered by a feedback between ice melt-back and subsidence to $O(10^{10})$ W, which is similar to observed power output, suggesting long-term stability. Turbulent dissipation makes testable predictions for the final flybys of Enceladus by *Cassini*. Our model shows how open connections to an ocean can be reconciled with, and sustain, long-lived eruptions. Turbulent dissipation in long-lived slots helps maintain the ocean against freezing, maintains access by future Enceladus missions to ocean materials, and is plausibly the major energy source for tiger stripe activity.

volcanism | astrobiology | icy moons | outer Solar System | Saturn

Enceladus' tiger stripes have been erupting continuously since their discovery in 2005 (1–4). The eruptions have been sustained for much longer than that: Saturn's E-ring, which requires year-on-year replenishment from Enceladus, has been stable since its discovery in 1966. Each of the four eruptive fissures is flanked by <1-km-wide belts of endogenic thermal emission (10^4 W/m for the ∼500-km total tiger stripe length), a one-to-one correspondence indicating a long-lived internal source of water and energy (5). The tiger stripe region is tectonically resurfaced, suggesting an underlying mechanism accounting for both volcanism and resurfacing, as on Earth. Enceladus' 30 ± 10-km-thick ice shell is probably underlain by an ocean or sea of liquid water, and Enceladus' plume samples a salty liquid water reservoir containing ^{40}Ar, ammonia, nano-silica, and organics (6–9). A continuous connection between the ocean and the surface is the simplest explanation for these observations. However, the consequences of this connection for ice shell tectonics have been little explored. The water table within a conduit would be ∼3.5 km below the surface (from isostasy), with liquid water below the water table, and rapidly ascending vapor plus entrained water droplets above. Condensation of this ascending vapor on the vertical walls of the tiger stripe fissures releases heat that is transported to the surface thermal-emission belts by conduction through the ice shell (Fig. 1) (1, 10–12). Because this vapor comes from the water table, there is strong evaporitic cooling of water $\lesssim 100$ m below the water table. Freezing at the water

table could release latent heat but would clog the fissures with ice in < 1 y. This energy deficit has driven consideration of shear heating, intermittent eruptions, thermal–convective exchange with the ocean, and heat engine hypotheses (5, 13, 14). It is easiest to explain the observations if the heat is made within the plumbing system.

The observed long-term steadiness of ice and gas output is modulated (for ice) by fivefold variability at the period $P = 33$ h of Enceladus' eccentric orbit about Saturn (the diurnal tidal period). Peak eruptive output anomalously lags peak tidal extension (by 5.1 ± 0.8 h relative to a fiducial model of the tidal response), and fissure eruptions continue from all four tiger stripes at Enceladus' periapse when all tidal crack models predict that eruptions should cease (1, 4, 11, 15). The sustainability of water eruptions on Enceladus affects the moon's habitability (e.g., ref. 16), as well as astrobiology (follow-up missions to Enceladus could be stymied if the plumes shut down). Despite the importance of understanding the sustainability of the eruptions, basic questions remain open: How can eruptions continue throughout the tidal cycle? How can the liquid water conduits obtain the energy to stay open—as needed to sustain eruptions—despite evaporitic cooling and viscous ice inflow? Why is the total power of the system ∼5 GW (not ∼0.5 GW or ∼50 GW)? Do tiger stripe mass and energy fluxes drive ice shell tectonics, or are the tiger stripes a passive tracer of tectonics?

We have found that a simple model of the fissures as open conduits can simultaneously explain both the maintenance of Enceladus' eruptions throughout the tidal cycle and the sustainability of eruptions on 10^{-1}-y to 10^1-y timescales, while predicting that eruptions are sustained over 10^6-y timescales. Fissures are modeled as parallel rectangular slots with length $L \approx 130$ km,

---

Significance

Eruptions on the ice moon Enceladus provide access to materials from Enceladus' ocean. The mechanism that drives and sustains the eruptions is unclear, and it is also not known what sets the rate of volcanism. We found that a simple model in which the erupting fissures are underlain by slots that connect the surface to the ocean can explain the observations. In the model, the slots are mostly filled with water, and Saturn tides drive turbulent water flow in the slots whose dissipation produces enough heat to keep slots open. In turn, long-lived water-filled slots drive a volcano-tectonic feedback that buffers the rate of volcanism to approximately the observed value. Our results suggest that the ocean–surface connection on Enceladus may be sustained on million-year timescales.

Fig. 1. The erupted flux from Enceladus (blue arrows) varies on diurnal timescales, which we attribute to daily flexing (dashed lines) of the source fissures by Saturn tidal stresses (horizontal arrows). Such flexing would also drive vertical flow in slots underneath the source fissures (vertical black arrow), which through viscous dissipation generates heat. This heat helps to maintain the slots against freezeout despite strong evaporitic cooling by vapor escaping from the water table (downward-pointing triangle). The vapor ultimately provides heat (via condensation) for the envelope of warm surface material bracketing the tiger stripes (orange arrows; "IR" corresponds to infrared cooling from this warm material).

depth $Z = 35$ km, stress-free half-width W_0, and spacing $S = 35$ km. Slots are connected to vacuum at the top, and open to an ocean at the bottom (Fig. 1 and *SI Appendix*). Subject to extensional slot-normal tidal stress $\sigma_n = (5 \pm 2) \times 10^4 \sin(2\pi t/p)$ Pa modified by elastic interactions between slots, the water table initially falls, water is drawn into the slots from the ocean (which is modeled as a constant-pressure bath), and the slots widen (Fig. 2). Wider slots allow stronger eruptions because the flow is supersonic and choked (17). Later in the tidal cycle, the water table rises, water is flushed from the slots to the ocean, the slots narrow, and eruptions diminish (but never cease) (Fig. 2). Solving the coupled equations for elastic deformation of the icy shell with turbulent flow of water within the tiger stripes allow us to compute $W(t)$ (*SI Appendix*). $W_0 > 2.5$-m slots oscillate in phase with σ_n, $W_0 < 0.5$-m slots lag σ_n by $\sim \pi/2$ rad, and resonant slots ($W_0 \sim 1$ m, tidal quality factor ~ 1) lag σ_n by ~ 1 rad (*SI Appendix*, Fig. S4). The net liquid flow feeding the eruptions (< 10 μm/s) is much smaller than the peak tidally pumped vertical flow (approximately ± 1 m/s for $W_0 \sim 1$ m, $Re > 10^5$). Although the amplitude of the cycle in water table height is reduced when the slot is hydrologically connected to the ocean relative to a hypothetical situation where the slot is isolated from the ocean, the flow velocity, driven by the deviation of the water table from its equilibrium elevation, is very much larger than in the hydrologically isolated case.

Turbulent liquid water flow into and out of the slots generates heat. Water temperature is homogenized by turbulent mixing, allowing turbulent dissipation to balance water table losses and prevent icing over. Ice forming at the water table is disrupted by aperture variations and vertical pumping; water cooled by evaporation, if sufficiently saline, will sink and be replaced by warmer water from below. A long-lived slot must satisfy the heat demands of evaporitic cooling at the water table (about $1.1\times$ the observed IR emission; *SI Appendix*) plus heating and melt-back of ice driven into the slot (18) by the pressure gradient between the ice and the water in the slot (19) (*SI Appendix*). Turbulent dissipation can balance this demand for $W_0 = (1 \pm 0.5)$ m, corresponding to phase lags of 0.5–1 rad, consistent with observations. Eruptions are then strongly tidally variable but sustained over the tidal cycle, also matching observations. $W_0 < 0.5$-m slots freeze shut, and $W_0 > 2.5$-m slots would narrow. Power output is sensitive to

the amplitude k of conduit roughness, which is poorly constrained for within-ice conduits. For the calculations in this paper, we use $k = 0.01$ m; for discussion, see *SI Appendix*. Near-surface apertures ~ 10 m wide are suggested by modeling of high-temperature emission (19), consistent with near-surface vent flaring (20). Rectification by choke points (18) [which are required to explain the absence of sodium in the gas plume (21)], together with condensation on slot walls, and ballistic fallback (6) could plausibly amplify the less than twofold slot-width variations in our model to the fivefold variations in the flux of ice escaping Enceladus. Water's low viscosity slows the feedback that causes the fissure-to-pipe transition for silicate eruptions on Earth (22, 23), which is suppressed for Enceladus by along-slot mixing (*SI Appendix*).

The mass and heat fluxes associated with long-lived slots (24) would drive regional tectonics (*SI Appendix*). Slow inflow of ice into the slot (25) occurs predominantly near the base of the shell, where ice is warm and soft. Inflowing ice causes necking of the slot, which locally intensifies dissipation until inflow is balanced by melt-back. Melt-back losses near the base of the shell cause colder ice from higher in the ice shell to subside. Because subsidence is fast relative to conductive warming timescales, subsidence of cold more-viscous ice is a negative feedback on the inflow rate. This negative feedback adjusts the flux of ice consumed by melt-back near the base of the shell to balance the flux of subsiding ice (*SI Appendix*, Fig. S6), which in turn is equal to the mass added by condensation of ice from the vapor phase above the water table (*SI Appendix*, Fig. S6). The steady-state flux of ice removed from the upper ice shell via subsidence and remelting at depth depends on Z, S, moon gravity, and the material properties of ice. Using an approximate model of ice shell thermal structure, this steady-state flux is approximately proportional to Z in the range 20 km $< Z < 60$ km (*SI Appendix*, Fig. S8) and is ~ 3 ton/s (7 mm/y subsidence, $Pe \approx 6$) for $Z = 35$ km. This long-term value for ice removal is comparable to the inferred post-2005 rate of ice addition to the upper ice shell, 2 ton/s [assuming the observed 4.4 ± 0.2 GW cooling of the surface is balanced by recondensation of water vapor on the walls of the tiger stripes above the water table (5, 11, 23, 26)]. If near-surface condensates are distributed evenly across the surface of the tiger

Fig. 2. Tidal flexing cycle for interacting slots assuming two inboard (*ib*) and two outboard (*ob*) slots, $E = 6$ GPa, and $L = 100$ km. Slot half-width $W_0 = 1$ m, wall roughness $k = 0.01$ m. ΔW_m is maximum width change, $\Delta V/V$ is fractional change in slot water volume, and σ_n is extensional stress to 90% of its own peak amplitude.
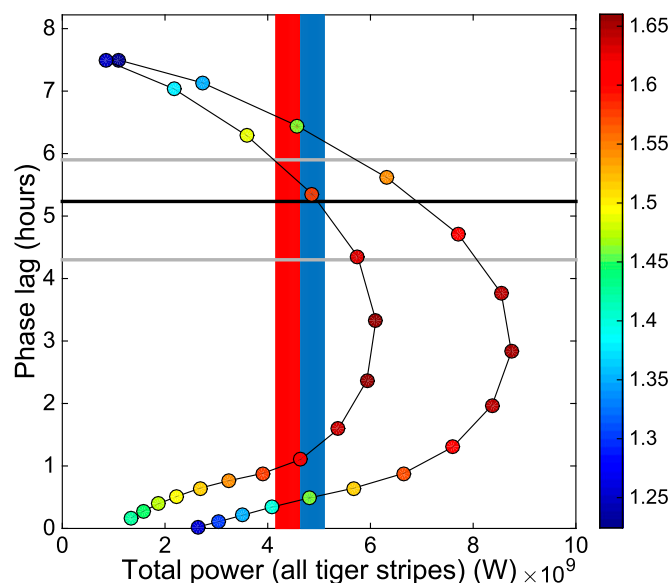
Fig. 3. Turbulent dissipation that can account for the observed power output of Enceladus (red bar; blue bar includes the additional power inferred for reheating of cold ice at depth) can also match the observed phase lag of Enceladus (thick black horizontal line shows phase lag relative to a fiducial model; gray lines show 1σ error in observed phase lag). Curves correspond to time-averaged power for (left curve) four slots of equal length of 100 km, and (right curve) 93-km length outboard slots and 151-km length inboard slots. Dot color corresponds to the fractional change in aperture (max/min) during the tidal cycle. For each curve, initial (tidal-stress–free) half-width is sampled at 0.125 m (uppermost dots), and then at 0.125-m intervals up to 2 m (lowermost dots). Half-widths that best fit both the phase delay and power constraints are 0.375–0.625 m.

stripe terrain [either by near-surface tectonics (27) or by ballistic fallback], then the balance is self-regulating because increased (decreased) tiger stripe activity will reduce (increase) the rate at which accommodation space for condensates is made available via subsidence in the near surface. This is consistent with sustained eruptions on Enceladus at the *Cassini*-era level over $>10^6$ y. Under these conditions, the ice is relatively cold and non-dissipative. In summary, turbulent dissipation of diurnal tidal flows (Fig. 1) explains the phase lag and the diurnal-to-decadal sustainability of liquid-water–containing tiger stripes (Fig. 3), and the coupling between tiger stripes and the ice shell forces a $>10^6$-y geologic cycle that buffers Enceladus' power to approximately the *Cassini*-era value.

Our model makes predictions for the results of *Cassini*'s final flybys of Enceladus. We predict that endogenic thermal emission will be absent between tiger stripes, in contrast to the region-wide thermal emission that is expected if the phase lag is caused not by water flow in slots, but instead by a $Q \sim 1$ ice shell (11, 28, 29). In our view, the tiger stripes are the loci of sustained emission because other fractures are too short ($L < 100$ km) for sustained flow. Because sloshing homogenizes water temperatures along stripe strike (*SI Appendix*), the magnitude of emission should be relatively insensitive to local tiger stripe orientation, a prediction that distinguishes the slot model from all crack models. Variations in thermal emission on 10-km length scales have been reported (e.g., ref. 1) and might allow this prediction to be tested. The slot model predicts a smooth distribution of thermal emission at the greater-than-kilometer scale. Our model is more easily reconciled with curtain eruptions (4) than jet eruptions (1), and it can provide a physical underpinning for curtain eruptions. Localized emission might still occur, for example near Y junctions. The pattern of spatial variability in orbit-averaged activity should be steady, in contrast to bursty hypotheses, and vapor flux should covary with ice-grain flux. Spatially resolved variability with orbital phase (1, 4) should correspond to the effects of water transfer along-slot, elastic interactions between slots and along slot walls, and possible along-slot width variations. Our basic model might be used as a starting point for more sophisticated models of Enceladus coupling fluid and gas dynamics (26), as well as the tectonic evolution and initiation of the tiger stripe terrain (e.g., ref. 29). Such coupling may be necessary to understand the initiation of ocean-to-surface conduits on ice moons including Enceladus and Europa, which remains hard to explain (30, 31). Initiation may be related to ice shell disruption during a past epoch of high orbital eccentricity: such disruption could have created partially water-filled conduits with a wide variety of apertures, and evaporative losses caused by tiger stripe activity would ensure that only the most dissipative conduits (those with $W_0 = 1 \pm 0.5$ m; Fig. 3) endure to the present day. Eccentricity variations on $>10^7$-y timescales may also be required if the ocean is to be sustained for the $>10^7$-y timescales that are key to ocean habitability (32–34). Ocean longevity could be affected by heat exchange with self-sustained slots in the ice shell. Testing habitability on Enceladus (or Europa) ultimately requires access to ocean materials, and this is easier if (as our model predicts) turbulent dissipation keeps the tiger stripes open for $\gg$ Kyr.

1. Porco C, DiNino D, Nimmo F (2014) How the jets, heat and tidal stresses across the south polar terrain of Enceladus are related. *Astron J* 148:45.
2. Hansen CJ, et al. (2011) The composition and structure of the Enceladus plume. *Geophys Res Lett* 38:L11202.
3. Dong Y, Hill TW, Teolis BD, Magee BA, Waite JH (2011) The water vapor plumes of Enceladus. *J Geophys Res* 116:A10204.
4. Spitale JN, Hurford TA, Rhoden AR, Berkson EE, Platts SS (2015) Curtain eruptions from Enceladus' south-polar terrain. *Nature* 521(7550):57–60.
5. Nimmo F, Spencer JR (2013) Enceladus: An active ice world in the Saturn system. *Annu Rev Earth Planet Sci* 41:693–717.
6. Postberg F, Schmidt J, Hillier J, Kempf S, Srama R (2011) A salt-water reservoir as the source of a compositionally stratified plume on Enceladus. *Nature* 474(7353):620–622.
7. Waite JH, Jr, et al. (2009) Liquid water on Enceladus from observations of ammonia and ^{40}Ar in the plume. *Nature* 460:487–490.
8. Iess L, et al. (2014) The gravity field and interior structure of Enceladus. *Science* 344(6179):78–80.
9. Hsu H-W, et al. (2015) Ongoing hydrothermal activities within Enceladus. *Nature* 519(7542):207–210.
10. Abramov O, Spencer JR (2009) Endogenic heat from Enceladus' south polar fractures: New observations, and models of conductive surface heating. *Icarus* 199: 189–196.
11. Nimmo F, et al. (2014) Tidally modulated eruptions on Enceladus: Cassini observations and models. *Astron J* 148:48.
12. Postberg F, et al. (2009) Sodium salts in E-ring ice grains from an ocean below the surface of Enceladus. *Nature* 459(7250):1098–1101.
13. Matson DL, et al. (2012) Enceladus: A hypothesis for bringing both heat and chemicals to the surface. *Icarus* 221:53–62.
14. Nimmo F, Spencer JR, Pappalardo RT, Mullen ME (2007) Shear heating as the origin of the plumes and heat flux on Enceladus. *Nature* 447(7142):289–291.
15. Hurford TA, et al. (2009) Geological implications of a physical libration on Enceladus. *Icarus* 203:541–552.
16. McKay CP, Anbar AD, Porco C, Tsou P (2014) Follow the plume: The habitability of Enceladus. *Astrobiology* 14(4):352–355.
17. Schmidt J, Brilliantov N, Spahn F, Kempf S (2008) Slow dust in Enceladus' plume from condensation and wall collisions in tiger stripe fractures. *Nature* 451(7179): 685–688.

18. Cuffey K, Patterson W (2010) *The Physics of Glaciers* (Elsevier, Burlington, MA), 4th Ed.
19. Goguen JD, et al. (2013) The temperature and width of an active fissure on Enceladus measured with Cassini VIMS during the 14 April 2012 South Pole flyover. *Icarus* 226: 1128–1137.
20. Mitchell K (2005) Coupled conduit flow and shape in explosive volcanic eruptions. *J Volcanol Geotherm Res* 143:187–203.
21. Schneider NM, et al. (2009) No sodium in the vapour plumes of Enceladus. *Nature* 459(7250):1102–1104.
22. Bruce PM, Huppert HE (1989) Thermal control of basaltic fissure eruptions. *Nature* 342:665–667.
23. Wylie JJ, et al. (1999) Flow localization in fissure eruptions. *Bull Volcanol* 60:432–440.
24. Howett C, et al. (2014) Enceladus' enigmatic heat flow. *Proceedings of the 46th Meeting of the Division for Planetary Sciences* (American Astronomical Society, Washington, DC), Abstract 405.02.
25. Röthlisberger H (1972) Water pressure in intra- and subglacial channels. *J Glaciol* 11: 177–203.
26. Ingersoll AP, Pankine AA (2010) Subsurface heat transfer on Enceladus: Conditions under which melting occurs. *Icarus* 206:594–607.
27. Barr AC, Preuss LJ (2010) On the origin of south polar folds on Enceladus. *Icarus* 208: 499–503.
28. Běhounková M, et al. (2015) Timing of water plume eruptions on Enceladus explained by interior viscosity structure. *Nat Geosci* 8:601–604.
29. Běhounková M, Tobie G, Choblet G, Čadek O (2012) Tidally-induced melting events as the origin of south-pole activity on Enceladus. *Icarus* 219:655–664.
30. Crawford GD, Stevenson DJ (1988) Gas-driven water volcanism in the resurfacing of Europa. *Icarus* 73:66–79.
31. Roth L, et al. (2014) Orbital apocenter is not a sufficient condition for HST/STIS detection of Europa's water vapor aurora. *Proc Natl Acad Sci USA* 111(48):E5123–E5132.
32. Meyer J, Wisdom J (2007) Tidal heating in Enceladus. *Icarus* 188:535–539.
33. Tyler R (2011) Tidal dynamical considerations constrain the state of an ocean on Enceladus. *Icarus* 211:770–779.
34. Thomas PC, et al. (2016) Enceladus's measured physical libration requires a global subsurface ocean. *Icarus* 264:37–47.

EARTH, ATMOSPHERIC, AND PLANETARY SCIENCES

Sustained eruptions on Enceladus explained by turbulent dissipation in tiger stripes: Supplementary Information

Edwin S. Kite[1] & Allan M. Rubin[2]

[1]Department of Geophysical Sciences,

University of Chicago, Chicago, IL 60637,

USA (kite@uchicago.edu).

[2]Department of Geosciences, Princeton

University, Princeton, NJ 08542, USA.

Appendix A: Supplementary Materials.

A1. Tidal stress cycle.

Enceladus is in 1:1 spin:orbit resonance with Saturn, but its eccentric orbit produces a time-varying (diurnal) stress cycle. We calculate $\sigma_n(t, \phi, \theta)$ for Enceladus' tiger stripes (where σ_n is extensional slot-normal tidal stress, t is time, ϕ is colatitude and θ is longitude) using a thin-shell approximation in which radial stresses, physical-libration stresses, obliquity stresses [1], nonsynchronous-rotation stresses, and tiger-stripe inter-actions are neglected [2, 3, 4]. We set the Poisson ratio to 0.33 and use fiducial Love numbers $l_2 = 0.04$ and $h_2 = 0.2$ for ease of comparison with previous work (e.g., [2]). High Love numbers are appropriate for a thin ice shell above a global ocean [5]. (Section A7 discusses sensitivity to l_2 and h_2). Tiger stripe locations are traced from http://photojournal.jpl.nasa.gov/catalog/PIA12783. The results (Fig. S1) show that stresses along the tiger stripes are generally "in phase" (Fig. S2), with peak com-pression near periapse. Therefore we approximate the tiger stripes as straight, parallel, and with in-phase forcing. The peak-to-trough amplitude of the stress cycle along the main tiger stripes is $(1.31 \pm 0.28) \times 10^5$ Pa. Sensitivity tests introducing $< 90°$ phase lags between stripes show no significant effect on time-averaged power.

A2. Slot width cycle.

Consider a thin shell of impermeable, isotropic ice I with thickness Z floating on a very voluminous water ocean. Stresses do not vary with depth within the shell, membrane stresses are neglected, and the ocean is treated as a constant-pressure bath. The shell is

perforated by one or more rectangular slots of length L and (initially) uniform half-width W_0 ($L \gg W_0$), with walls of roughness k (Fig. S3). For the slot calculations we neglect curvature (adopting Cartesian geometry) and assume plane stress. Plane stress is more reasonable for Enceladus' tiger stripes than plane strain: $L = $ 90-190 km (from imaging), whereas Z is most likely 30-40 km and very probably $\leq$ 60 km [6].

Water rises within the slot to $D \approx \frac{\rho_i}{\rho_w} Z$, where $\rho_i = $ 916 kg/m^3 is ice density and $\rho_w = $ 1000 kg/m^3 is water density. Ocean over-pressure [7] or siphoning of the water by bubbles could raise the mean water table, but this would have only a small effect on our diurnal-cycle results. (Liquid water is not seen at the surface, suggesting that the ocean is not currently over-pressured by more than 0.3 MPa.) The slot is assumed to have adjusted prior to $t = 0$ through freezing and melt-back so that at $t = 0$ the slot width is uniform with depth.

The ice slab is subject to periodic, extensional, slot-normal stress $\sigma_n = \frac{A}{2}\sin(n_f t)$ where A is the peak-to-trough amplitude of the diurnal tidal stress cycle, $n_f = 2\pi/p$, and $p \sim$ 33 hours is the period of Enceladus' orbit. Sinusoidal time dependence is valid for small orbital eccentricity.

In the absence of water, and assuming linear elasticity, the plan-view slot area for a single slot (Y) oscillates in phase with the forcing:

$$Y(t) = 2W_0 L + \frac{\pi}{2} L \Delta W_m = L\left(2W_0 + \frac{\pi \sigma_n L}{2E}\right) \tag{A1}$$

where E is the Young's modulus of ice ($\sim 6 \times 10^9$ Pa [8, 9]), and ΔW_m is the change in half-width at the location of greatest (maximum) half-width change. This is because $\Delta W(y_*)$

$= 2\,\sigma_n E^{-1} \sqrt{(L/2)^2 - y_*^2}$ where y_* is distance along-slot measured from the middle of the slot length [10].

Adding viscous fluid modifies the tidal cycle in Y. Conservation of water volume during a single tidal cycle relates changes in ΔW and volume exchange with the ocean:

$$\frac{\partial \Delta W_m}{\partial t}\left(\frac{\pi L}{2}\right)(D+h) + \frac{\partial h}{\partial t}\left(2W_0 L + \frac{\Delta W_m \pi L}{2}\right) = Q \tag{A2}$$

where h is the time-varying part of the water level and Q corresponds to influx at the slot base. We assume $h \neq h(y)$, which is reasonable for Enceladus (§A.2, §A.6, §A.10), and we neglect terms of order h/z or $(z-D)/z$. The first term on the left-hand side accounts for width change, and the second term accounts for changes in h. Slot-wall freeze-on and melt-back has characteristic timescale $\gg p$ (§A.6). h is set by the time-varying normal stress that would act across the crack in the absence of relative motion of the crack walls (σ_∞) as modified by the crack-wall stress perturbation due to relative motion (σ_{el}):

$$\rho_w g h = -\sigma_\infty - \sigma_{el} = -\frac{A}{2}\sin(n_f t) + \Delta W_m(t)\frac{2E}{L} \tag{A3}$$

where the pressure distribution within the water column responds to changes in far-field stresses or in water volume on timescale $\ll p$ (inertia is unimportant).[1] Differentiating,

$$\rho_w g \frac{\partial h}{\partial t} = -n_f \frac{A}{2}\cos(n_f t) + \frac{\partial \Delta W_m(t)}{\partial t}\frac{2E}{L} \tag{A4}$$

Substituting,

$$\left(D + \frac{1}{\rho_w g}\left(-\frac{A}{2}\sin(n_f t) + \frac{\Delta W_m E}{L/2}\right)\right)\frac{\partial \Delta W_m}{\partial t}\left(\frac{\pi L}{2}\right) +$$
$$\frac{1}{\rho_w g}\left(-n_f \frac{A}{2}\cos(n_f t) + \frac{\partial \Delta W_m}{\partial t}\frac{2E}{L}\right)\left(2W_0 L + \frac{\pi L \Delta W_m}{2}\right) = Q \quad \text{(A5)}$$

Rearranging,

$$\frac{\partial \Delta W_m}{\partial t} = \frac{4g\rho_w Q + 4n_f L W_0 A\cos(n_f t) + \pi n_f L \Delta W_m A\cos(n_f t)}{16EW_0 + 8\pi E\Delta W_m - \pi L A\sin(n_f t) + 2\pi g\rho_w DL} \quad \text{(A6)}$$

As a check we run $Q = 0$, $W_0 = 1$ m. This corresponds to a slot that contains water, but is hydrologically isolated from the ocean. We find $\Delta W_m \sim 0.02$ m, as expected, which would lead to negligible tidal flow within the slot and negligible viscous heat generation. However, hydrological connections to the ocean are suggested by the observation of ocean material in the plume [12, 13, 14].

Solving (A6) requires requires $Q(t) = Y(t)V(t)$ (V is velocity), but first we consider interactions between slots.

A3. Slot-slot interactions.

The tiger stripes are $S \sim 35$ km apart and $L \sim 130$ km long (stripes can be mapped using images of the surface or alternatively using the trace of individually triangulated supersonic ice sources; L is slightly shorter for the second approach), so elastic interactions between slots can be important (Fig. S1). We model interactions using a two-dimensional displacement discontinuity implementation of the boundary element method [15, 16], with plane stress, neglecting planetary curvature. Using this code, we investigated interactions between slots of a variety of geometries, branching patterns, and lengths. The tiger stripes

71   are reasonably well-approximated as being straight, parallel, equally spaced (Fig. S1) and

72   in phase (Fig. S2). With those approximations, the tiger stripe terrain is essentially

73   symmetric, so that the deformation cycle for the Alexandria and Damascus Sulci (the

74   outboard slots) will be the same, and the deformation cycle for the Baghdad and Cairo

75   Sulci (the inboard slots) will be the same. However, the deformation cycle for the outboard

76   slots will differ from that for the inboard slots. Because slot width is much less than tiger-

77   stripe spacing, the coupling terms are insensitive to both possible between-slot variations

78   in mean width and possible along-slot variations in width.

79   We can write the stress change that would occur on the walls of the perturbed stripe-pair

80   if those walls were not free to move as follows:

$$\Delta P_{ij} = \frac{\Delta w_i}{\left(\frac{\partial w_i}{\partial p_i}\right)} \left(\frac{\partial w_j}{\partial p_i}\right) \left(\frac{\partial p_j}{\partial w_j}\right) = \left(\frac{\partial p_{j,iso}}{\partial w_{j,iso}}\right) r_{ij} \Delta W_{m,i} \qquad (A7)$$

81   where the subscript i corresponds to the perturbing stripe-pair, the subscript j corresponds

82   to the perturbed stripe-pair, and the subscript *iso* corresponds to deformation of a *single*

83   slot of length equal to j. ($\partial p_{iso}/\partial w_{iso} = 2E/L$ for a straight slot.) We average over

84   slot plan-view shape variations by defining w as the along-slot average width of the slot.

85   (This averaging anticipates the along-slot averaging in our discharge-velocity calculation,

86   §A.4). The second term in brackets ($\partial w_j/\partial p_i$) evaluates the thickness change of j due

87   to a pressure change at i for the case of constant stress within j, i.e. allowing the walls

88   of j to undergo relative motion. Δw_i is found iteratively, and all other terms are pre-

89   computed using the two-dimensional displacement-discontinuity boundary element code.

Elastic interactions are rapid relative to the tidal cycle (the sound-crossing timescale $(3S/v_{sound}) = (10^2 \text{ km}/4 \text{ km s}^{-1}) \approx 30 \text{ s} \ll p)$.

To take account of interacting slots, (A3)-(A6) must be modified. For one of a pair of cracks (i) that interacts with another pair (j), $\sigma_{\infty,i}$ must be modified to include the normal stress perturbation on i due to relative motions of the walls of j (enforcing zero relative motion of the walls of i), while $\sigma_{el,i}$ must be modified to account for the other of the i pair. We obtain (by analogy with A3-A6)

$$\sigma_{\infty,i} = \frac{A}{2}\sin(n_f t) + \frac{2E}{L}r_{ji}\Delta W_{m,j}$$

$$\sigma_{el,i} = \frac{2E}{L}r_{ii}\Delta W_{m,i}$$

$$\rho_w g h_i = -\frac{A}{2}\sin(n_f t) + \frac{2E}{L}(r_{ii}\Delta W_{m,i} - r_{ji}\Delta W_{m,j})$$

$$\left(D + \frac{1}{\rho_w g}\left(-\frac{A}{2}\sin(n_f t) + \frac{2E}{L}\left(r_{ii}\Delta W_{m,i} - r_{ji}\Delta W_{m,j}\right)\right)\right)\frac{\partial \Delta W_{m,i}}{\partial t}\left(\frac{\pi L}{2}\right) + \frac{1}{\rho_w g}\left(-n_f\frac{A}{2}\cos(n_f t) + \frac{2E}{L}\left(r_{ii}\frac{\partial \Delta W_{m,i}}{\partial t} - r_{ji}\frac{\partial \Delta W_{m,j}}{\partial t}\right)\right)\left(2W_0 L + \frac{\pi L \Delta W_{m,i}}{2}\right) = Q_i$$

and rearranging yields an implicit equation analogous to (A6):

$$\frac{\partial \Delta W_{m,i}}{\partial t} = \frac{Q_i + (\rho_w g)^{-1}\left(\frac{1}{2}A n_f \cos(n_f t) + \frac{2}{L}E r_{ji}\frac{\partial \Delta W_{m,j}}{\partial t}\right)Y}{\frac{1}{2}L\pi\left(D - (\rho_w g)^{-1}\left(\frac{1}{2}A\sin(n_f t) - \frac{2E}{L}(r_{ii}\Delta W_{m,i} - r_{ji}\Delta W_{m,j})\right)\right) + \frac{2E r_{ii} Y}{L g \rho_w}}$$

(A8)

where r_{ii} corresponds to the interaction between paired tiger stripes, and r_{ji} corresponds to the interaction between the outboard slot pair and the inboard slot pair (we use r_{ji} to refer to the influence of the motion of slot i on j). The r terms are computed for uniform stress changes within the slots, consistent with the the assumption of in-phase

tidal loading. When the deformation is in phase between paired tiger stripes, r_{ii} is in the

range $0 < r_{ii} < 1$ (deformation-promoting) and r_{ji} is negative (deformation-retarding).

For the solutions that match data (Fig. 2), the slots track each other within 20% of

power output and within 1 hr in phase. However, the slot-pairs can deform very differently

for parameters that may be encountered during Enceladus' geologic evolution (§A.7).

Interactions between slots may be relevant to the origin of the parallel, equally-spaced

tiger stripes: once a slot is established, it will produce bending stresses in the adjacent

shell that favor failure at horizontal distances approximately equal to the shell thickness

(e.g., [32]). This preferred wavelength is found for icebergs on Earth [17].

A4. Turbulent viscous dissipation.

Extensional (compressional) stress causes h to fall (rise) which draws water into

the slot from the ocean (expels water from the slot into the ocean). Veloc-

ity V at the slot inlet depends on the pressure gradient ∇P, the roughness of

the slot walls k, and the Reynolds number Re. Here we linearize by assuming

$\nabla P \sim (D + h)^{-1}(\sigma_n(t) - 2(r_{ii}\Delta W_{m,i} - r_{ji}\Delta W_{m,j})E/L)$. Velocities normal to the crack

wall are much smaller than velocities parallel to the crack wall, and we also ignore flow

parallel to the long axis of the tiger stripes ; in detail the pressure gradient will be af-

fected by (and feed back on) slot-width variations with depth in the shell. Combining the

Darcy-Weisbach and Colebrook-White equations gives ([18], their Equation 4.10):

$$|V| = -2\sqrt{2g_E dS_f} \, \log_{10} \left(\frac{k}{3.7d} + \frac{2.51\nu}{d\sqrt{2g_E dS_f}} \right) \tag{A9}$$

where g_E is Earth gravity, S_f is the dimensionless energy loss gradient ($S_f = \nabla P_z/\rho g_E$), $\nu \approx 1.8 \times 10^{-6}$ m^2 s^{-1} is the kinematic viscosity of water at $0°$ C, and we set the equivalent pipe diameter d to be 4 times the mean slot half-width $W^*_{1/2}(t) = \frac{1}{2}\left(2W_0 + \frac{\pi}{2}\Delta W_m\right)$. The first term inside the brackets accounts for rough turbulent flow, which dominates for $|V| \sim 1$ m/s, $k > 0.001$ m (Enceladus-relevant conditions), so

$$|Q| \approx -4LW^*_{1/2}\sqrt{2g_E(4W^*_{1/2})\left|\frac{\Delta P}{\left(D - \Delta P\frac{1}{\rho_w g}\right)}\frac{1}{\rho_w g_E}\right|}\log_{10}\left(\frac{k}{14.8W^*_{1/2}}\right) \qquad (A10)$$

where

$$\Delta P = \left(\frac{A}{2}\right)\sin(n_f t) - (r_{ii}\Delta W_{m,i} - r_{ji}\Delta W_{m,j})2E/L \qquad (A11)$$

and we have again linearized the pressure gradient. The sign of Q (positive for inflow into the slot) is set equal to the sign of ∇P.

We now have an expression for Q which can be substituted in (Eqn. A8) to solve for $\Delta W_m(t)$. By multiplying Q by the magnitude of the pressure difference between the ocean and the slot, we obtain an estimate of $F(t)$, the average power dissipated per length of tiger stripe (see §A.10 for a more detailed discussion). An alternative approach (from [19], their Fig. 2.11) gives the nondimensional average pressure gradient ξ as the maximum of ξ_l (laminar) and ξ_t (turbulent)

$$\xi = \max(\xi_l, \xi_t)$$

$$\xi_l = 32Re$$

$$\xi_t = 0.25Re^{\sim 1.75} \qquad (A12)$$

where $Re = 2W^*_{1/2}(t)\, V(t)\, /\, \nu$. The power per unit length (W/m) is then ([19], their Fig. 2.11)

$$F \approx |V| \frac{D\xi\mu^2}{\rho_w(2W_0 + (\pi/2)\Delta W_m)^2} \tag{A13}$$

where we neglect the difference between D and $D + h$, assume a static pressure gradient, and advect water parcels through the gradient at speed $|V|$. μ is the dynamic viscosity of water ($\mu = \nu\, \rho_w$). We find that (A9-A10) gives the same power output as (A13) for $k \approx 0.02$ m, $W_0 = 1$ m.

Most of this power will go (at steady state) into evaporative losses at the water table or into the ice, rather than being mixed into the ocean: heat flow scales as $1/\delta_{bl}$, and boundary layer thicknesses δ_{bl} are small within the slot. In addition, heated water is buoyant relative to cold water of the same salinity (for salinity > 2 %, which is plausible for Enceladus waters that have undergone fractional evaporation) so it will remain under the slots (either as a sheet, or concentrated in cupolas beneath slots). The total power for the slot is $LF(t)$, and because the change in water temperature during one tidal cycle is $\ll 1$ K, the diurnal-mean F is used to compare to observations (Figs. 2-3).

Fig. S4 shows results for uncoupled slots, $W_0 = \{0.25, 0.375, 0.5, ...2.5\}$ m, $L = 100$ km, $S = Z = 35$ km.

Fig. S5 shows results for coupled slots of equal length, $W_0 = \{0.25, 0.375, 0.5, ...2.5\}$ m, $L = 100$ km, $S = Z = 35$ km.

A5. Ice inflow and melt-back

152 In isostatic equilibrium, a differential stress σ_x drives viscous ice inflow into the slot

153 (Fig. S6) [20]. σ_x reaches a maximum of $g\rho_i(Z-H)$ at the water table, where $g \approx 0.1$ m/s^2

154 is Enceladus gravity, and tapers linearly to zero at the moon's surface and at the ocean

155 inlet. The corresponding ice-divide strain rate, $\dot{\epsilon}_{xx}(z)$, is given by

$$\dot{\epsilon}_{xx}(z) = \frac{1}{8}N(T)\sigma_x(z)^3 \tag{A14}$$

156 where $N(T)$ is the creep parameter of ice I and the factor of 1/8 assumes confinement in

157 the along-slot (y) direction [[21], p. 62]. Solid-ice flow is much slower than the oscillating

158 liquid-water flow in the slot. Most of the flow will occur for $T > 200$K, $\sigma_x \sim 10^5$ Pa,

159 and for these conditions $N(T)$ is well-constrained (these flow conditions correspond to

160 terrestrial ice sheets). To solve for $\dot{\epsilon}_{xx}(z)$, we first calculate the ice inflow rate with a

161 conductive geotherm:

$$T(z) = T_s + (T_m - T_s)(z/Z) \tag{A15}$$

162 with Enceladus surface temperature $T_s = 60$K and ice-shell base temperature $T_m = 273$K.

163 We log-linearly interpolate $N(T)$ from Table 3.4 in [21] and approximate the inflow rate

164 $v_x(z)$ as the product of $\dot{\epsilon}_{xx}(z)$ and the half-width between tiger stripes, $S/2$. This gives

165 a peak ice inflow rate of 0.3 m/yr and a depth-averaged ice inflow rate $(\overline{v_x})$ of 0.04

166 m/yr. However, this is not yet a self-consistent setup. That is because such high ice

167 inflow rates cause rapid subsidence of cold ice from above, which perturbs the geotherm,

168 lowering $T(z)$ [22]. Meanwhile, the water-filled slot defines an isothermal, relatively warm

169 vertical boundary condition. To take account of these competing effects, we use a 2D

170 conduction-advection code [23] to find temperatures within the ice shell as a function of

171 a dimensionless Péclet number λ_z.

$$\lambda_z = \frac{\rho_i c_p v_z Z}{k_i} \qquad (A16)$$

172 where $v_z = 2\,\overline{v_x}$ (for $S = Z$) is the subsidence rate, $c_p = 2000$ J/kg/K is ice heat capacity,

173 and $k_i = 2.5$ W/m/K is ice thermal conductivity. We assume $v_z \neq v_z(z)$, in effect assum-

174 ing that horizontal flow is concentrated near the base of the slot (this will be justified a

175 posteriori). Then we take the v_z implied by the conductive solution, and use (A16) to

176 get λ_z, find the corresponding ice-divide temperatures in the 2D model output, and use

177 (A14) to find the new $v_x(z)$. Iteration gives a steady state: $\overline{v_x} = 3.4$ mm/yr ($Pe_z \sim 6$),

178 peak $v_x = 3$ cm/yr, melting losses $= 2\overline{v_x}l_{melt}\rho_i Dl \approx 10^8$ W per slot, sensi-

179 ble heat losses $= 2\overline{v_x}(273\text{K} - 60\text{K})c_p\rho_i Dl \approx 10^8$ W per slot (Fig. S7). (Here,

180 $l_{melt} = 334$ kJ/kg is the latent heat of fusion of water). At steady state, with these

181 approximations, 90% of the inflow comes from the lowermost 20% of the ice shell, which

182 validates the approximation $v_z \neq v_z(z)$ made above. Faster ice inflow near the base of the

183 shell will narrow the slot at its base, until local enhancement of turbulent dissipation in

184 the liquid-water slot at the narrowed ocean inlet generates enough melt-back to balance

185 inflow.

186 Ice loss by melting near the base of the ice shell is balanced (at steady state) by ice

187 gain near the top of the ice shell by condensation and by frost accumulation. In a hori-

188 zontal average, subsidence creates accommodation space for the near-surface build-up of

189 condensates (an inevitable consequence of tiger stripe activity, that would otherwise be

190 expected to plug up conduits). The distribution of condensates across the ice surface de-

191 pends on the poorly-understood mechanics of the uppermost kilometer of Enceladus' ice

192 shell [24, 25, 26, 27], and on the long-term average partitioning of condensates between

193 ballistic rainout and fissure-wall condensation [28]. Because water vapor gives up the

194 latent heat of sublimation l_{subl} upon condensation to ice, we predict a total (four-stripe)

195 tiger stripe terrain thermal emission of $4 \; l_{subl} \; v_z \; \rho_i \; L \; S \approx 8$ GW for $Z = 35$ km. The ob-

196 served value is ~ 5 GW including the latent heat represented by the vapor escaping from

197 Enceladus. The short-term observed output is within a factor of ~ 1.6 of the predicted

198 long-term output for $Z = 35$ km.

199 Encouragingly, this roughly correct prediction of the power output of Enceladus requires

200 only S, Z, g, and the material properties of ice. The predicted power output scales as

201 $Z^{\approx 1}$ and intersects the observations at $Z = 25$ km (Fig. S8). The dependence of power

202 output on Z has the right sign to provide a negative feedback on ice shell thickness.

203 Ice sheets on Earth deform at rates fit by (A14) with $N(T)$ between $1\times$ and $5\times$ values

204 inferred from laboratory experiments (rheological compilation by [21]). Variations within

205 this range have remarkably little effect on the Enceladus steady-state power output. This

206 buffering suggests that a more sophisticated model of the depth-dependent creep pa-

207 rameter of the ice prism (which might include visco-elasto-plastic rheology, temperature-

208 dependent thermal conductivity, and 3D effects) would not greatly alter the equilibrium

209 values found here.

In steady-state geyser tectonics, processes that are not directly observed (melt-back and ice warming) contribute only $(l_{melt}+(273K-60K)c_p)/(l_{vap}+l_{melt}+(273K-60K)c_p) \approx 20\%$ of the energy demand that is balanced by viscous dissipation. This additional energy corresponds to the offset between the blue and red bars in Figs. 2 and 3. If we are wrong and the tiger stripe terrain has not yet reached tectonic steady state, then the power demand is higher because the bulk inflow rate is greater, but within the envelope of power that can be produced by turbulent dissipation (Fig. 2). [29] report 4.6±0.2 GW (since revised to 4.4±0.2 GW) of excess thermal emission from the tiger stripe terrain - corresponding to a desublimation flux of 1700 kg/s if all of the IR energy is supplied by desublimation. In addition, [30] report 200 kg/s of water vapor exiting the moon. Adopting $l_{vap} = 2.3 \times 10^6$ J/kg and $l_{melt} = 3.3 \times 10^5$ J/g, the directly constrained energy demand is 4.9±0.2 GW. This corresponds to the red bars in Figs. 2 and 3. In our model, at steady state 2.9×10^5 J/kg [21] are needed to re-heat cold ice from surface temperatures (∼60K) to 273K.

A6. Stability of slots.

Slot geometry is maintained through evening-out of temperature by along-slot stirring. Stirring is driven by along-slot gradients in the amplitude of diurnal cycles in slot width and flow velocity. These cycles have (for basic slot geometries) peak amplitude near the middle of the slot. Gradients from the middle to the ends of each slot, together with minor along-slot tidal phase variations (Fig. S2), drive bulk along-slot flow with velocity $O(10\%)$ that of the vertical flow. Because flow within the slot is turbulent, the effective stirring timescale is $O(10\%)L/\overline{V} \sim 40$ days. Currents in the ocean (which have been

231   calculated at $u > 1$ cm/s for Europa; [31]) will sweep water along the base of the slot

232   during the compressive phase of the cycle prior to re-ingestion during the tensile phase

233   of the cycle, and this will help to equalize temperatures within the slot on a timescale

234   L/u (~ 100 days for $u = 1$ cm/s).

235   These stirring timescales are short compared to the timescales for both melt-back and

236   slot-narrowing via inflow, and this helps to explain why the tiger stripes do not suffer end-

237   freezing nor undergo a corrugation instability. An upper bound on melt-back speed comes

238   from complete dissipation of the tidal stress cycle in the water, for which power per unit

239   volume is $2A/p = 2$ W/m^3. The corresponding timescale for melt-back doubling of the

240   width of a 1m-wide slot is not less than 1600 days. Halving of slot width by viscous inflow

241   of wall ice also takes much longer than along-slot isothermalization by stirring (§A.5). This

242   ratio of timescales favors suppression of the fissure-to-pipe transition. This contrasts with

243   magmatic fissures on Earth, for which along-slot thermal homogenization timescales are

244   long compared to freeze-out timescales. As a result, fissure eruptions develop into pipes

245   on Earth. Although a full treatment of instabilities in melt-back will require detailed

246   modeling, this heuristic argument suggests that long-lived fissure eruptions on Enceladus

247   are physically reasonable [33].

248   This argument for slot stability conservatively ignores ice-bridge disruption by strike-slip

249   motion ($O(1$ m$)$ per cycle; [3]), which could arrest the conversion of slots to pipes. If pipes

250   do form, they should be short-lived: pipes change their cross-sectional area by a fraction

251   of only $(A/E) \sim 10^{-5}$ during a tidal cycle, so unless the ocean's pressure undergoes a

252   high-amplitude diurnal pressure cycle, turbulent dissipation of diurnal flow within pipes

253 will be minor and the pipes should quickly freeze. Short-lived pipes may correspond to

254 patches of enhanced emission that have been reported in some analyses of *Cassini* images

255 (e.g. [32]); along-slot variations in the unfrosted width of fractures about the water table

256 are more consistent with a more recent analysis [33], that does not require pipes.

257 We have treated the ocean as a constant-pressure bath and ignored feedbacks of flushed

258 water on ocean pressure, which could be significant.

259 Fig. 2 in the main text shows how slots can be stable to changes in mean width: on the

260 branch where increases in W_0 reduce power output, if dissipation is too low, water will

261 freeze at the margins, narrowing the slot until a steady state can be reached. Similarly, if

262 dissipation is too high, the melt-back rate will increase, widening the slot until a steady

263 state can be reached.

264 At steady state, the latent heat of vapor escaping the water table must be balanced

265 by heat supplied from the water. Vertical resupply is assisted by exsolving, ascending

266 bubbles [34]. The km-scale changes in h help: some of the vapor is supplied from ice that

267 is warmed during the time that it is underwater, rather than directly from the water. The

268 changes in water level and in slot width also help to break up any ice that does form.

269 Evaporation makes the water at the top of the slot more salty, favoring subsidence. As

270 slot water evolves to salinity >2 wt%, cooled water would sink even supposing salt content

271 is not increased during evaporation. These processes will buffer water near the top of the

272 slot to modestly elevated salinity.

273 Observed thermal emission, if conductive, averages over 10^3 yr timescales because the

274 conductive path length from the fissure walls to the center of the thermal-emission belts is

275 hundreds of meters [35]. Thus, the fact that thermal emission from the four tiger stripes is

276 comparable indicates that the spacecraft-era continuity of activity from all four stripes is

277 representative of activity on 10^3 yr timescales. The fact that the emission is of the same

278 order of magnitude for the four tiger stripes further suggests a regulating mechanism

279 maintaining the stripes at that power - for example, turbulent dissipation (Fig. 2).

A7. Sensitivity tests and extensions.

280 F scales as σ_n^2, and σ_n increases with Love numbers h_2 and l_2; h_2 and l_2 are in turn

281 sensitive to uncertainties in internal structure [36, 37, 38] (Fig. S9). For example, one

282 recent analysis of *Cassini* gravity data gives $z \leq 25$ km at the tiger stripes [5]. Using the

283 h_2 and l_2 obtained for a thickness of 24 km by [36], the phase lag is reduced by 1.6 hours

284 relative to the fiducial model employed by [37]. Diurnal stresses and power output are

285 reduced (Fig. S9). Although libration indicates a global ocean and is consistent with high

286 h_2 and l_2 [39], the remaining uncertainty in Enceladus' true h_2 and l_2, and the averaging

287 steps in our turbulent power output estimation procedure, mean that agreement between

288 model-predicted peak power and *Cassini* data may be partly coincidental; nevertheless it

289 is encouraging that model predictions bracket the data.

290 F increases as surface roughness decreases (Fig. S10). Although we are not aware of

291 any k measurements for englacial channels with bi-directional flow, data and modeling

292 of supraglacial channels suggest $k <\sim 0.01$ m (e.g. [40], where we use [41] to convert

293 between the Manning coefficient and D_{50} and assume $D \sim k$).

$F \propto L^{\sim 3}$, provided that slots do not interact elastically (Fig. S11). Eruptions appear most concentrated from the central-most 100 km of the tiger stripes [33]. Power output for four equal-length 100 km slots is shown in Fig. 2 (left curve).

Nonlinear effects become important for large L for pairs of slots that interact elastically. Here again $F \propto L^{\sim 2}$ is expected, but nonlinear effects become important for large L. Consider two slots (or two pairs of slots) i and j whose walls are subject to time-varying internal pressure and which interact through elastic stresses. Neglecting the relatively minor contribution from the $\frac{\partial \Delta W_{m,j}}{\partial t}$ terms, the equations of motion can be written as:

$$\frac{\partial \Delta W_{m,i}}{\partial t} \sim Q_i + k_1 F(t) + k_2 F(t)(r_{ii}\Delta W_{m,i} - r_{ji}\Delta W_{m,j})$$

$$\frac{\partial \Delta W_{m,j}}{\partial t} \sim Q_j + k_3 G(t) + k_4 G(t)(r_{jj}\Delta W_{m,j} - r_{ij}\Delta W_{m,i}) \qquad \text{(A17)}$$

and the matrix of coupling coefficients is

$$\begin{pmatrix} r_{ii} & -r_{ij} \\ -r_{ji} & r_{jj} \end{pmatrix}$$

where the r terms are calculated using the output of a boundary-element code (§A.3). $|r_{ij}|$ becomes larger relative to $|r_{ii}|$ as the ratio of tiger stripe spacing to tiger stripe length increases. For slots of the observed length of Enceladus' tiger stripes (Fig. 2), the solution is stable.For sufficiently long or close-spaced slots the determinant of the coupling matrix becomes negative, and the coupled equations define a saddle-node instability. This instability manifests in the full equations as water piracy. During water piracy, one slot swells, with large-amplitude oscillations, and the other loses almost all its water and undergoes small-amplitude oscillations. The pirated slot would eventually become inactive due to reduced turbulent dissipation. Water piracy might limit the size both of

Enceladus' tiger stripe terrain and of the three tectonized regions of Miranda, which taken together have angular diameters $(70\pm10)°$, $n = 4$. That is because slots beyond a certain length would suffer destructive interference (if we suppose that the spacing of slots is set by the thickness of the ice shell). Salts on the surface of Europa suggest that conduits link Europa's surface to its sub-ice ocean [42], and if long water-filled slots on Europa destructively interfered, then this would affect the sustainability of activity [43]. The importance of tidal flexing to double ridges on Europa has previously been hypothesized by [44].

A8. Links to very long timescales.

Our model assumes that tidal heating powers Enceladus, consistent with previous work [45, 46, 47, 48, 49, 50, 51].

On timescales longer than the tectonic-resurfacing timescale for the South Polar terrain ($<10^6$ yr, from crater counts), orbital dynamics require that at least one of the following are true: (1) Enceladus' surface power output is intermittent [52]; (2) the tidal dissipation quality factor of Saturn is $<1.8 \times 10^4$, and the mid-sized icy satellites of Saturn are much younger than 4.5 Gyr [53].

Our work does not address this Gyr-timescale, "deep" problem of sustaining ocean-fuelled eruptions on Enceladus. We have focused instead on the "shallow" problem of how the eruptions, liquid-water plumbing system, and ice shell tectonics are interrelated at timescales from the 10^1 yr observational baseline up to the tiger-stripe terrain's tectonic refresh timescale ($4LSZ\rho_i l_{subl}/5\,\mathrm{GW} \approx 10^7$ yr). Beyond the tectonic refresh time geologic

331 information is lost, although terrains far from the tiger stripes [54] may record Enceladus'

332 activity at earlier times.

333   Of the subset of erupted water that goes into orbit around Saturn, very little returns

334 to the tiger stripe terrain. Therefore, if strict steady state in the ice shell is to be main-

335 tained, mass escaping from Enceladus should be balanced by mass supplied by the ocean.

336 Tracking changes in ocean volume over millions of years is beyond the scope of this study,

337 but the worst-case imbalance – supposing that water escaping from Enceladus is entirely

338 sourced from the ice shell, with zero replacement – is only $\sim$10% (200 kg/s escapes,

339 1700 kg/s circulates).

A9. Typical velocities within the slot are not much less than the velocity at the slot outlet.

340 Our equations assume the pressure distribution within the slot is linear, so that the flow

341 within the slot is given by a single representative velocity that is not much different from

342 the velocity at the slot outlet. In this section we show that this uniform-pressure-gradient

343 approximation does not affect our conclusion that turbulent dissipation can account for

344 the observed power output of Enceladus.

345   Flow in the slot is driven by the significant pressure gradient as the water table is

346 displaced from its equilibrium height. In the limit that the water provides negligible

347 resistance to flow (inertial or viscous), the water table remains stationary during the tidal

348 cycle. Given the tidal stress amplitude of $\sim$100 kPa (peak-to-trough), crack length of

349 $\sim$100 km, and Young's modulus of 6 GPa for ice, the slot width change for no pressure

350 (water table) change within the slot is $\sim$1.7 m. From $\partial V/\partial z = (\partial W/\partial t)/W$, with $V = 0$

351 at $z = 0$, $\Delta W \sim W$, $\Delta t \sim$ 16 hrs (1/2 tidal cycle), the velocity at the inlet is of order

0.5 m/s, and the average velocity in the slot half that. In the full solution (equation A6 or A8), the water does provide resistance to flow (this also generates the observed phase lag), such that the water table is displaced between the extreme values that arise from assuming an isolated slot ($\sim$0.5 km for W=1 m) and from assuming no resistance to flow (0 m). For our "best fitting" results, arising from an equilibrium half-thickness slightly less than 1 m, the water table is displaced of order 100 m and the flow velocity at the entrance is of order 0.4 m/s.

The pressure distribution with height within the slot can be derived as follows. Let $z = 0$ be the equilibrium height of water in slot (hydrostatic balance with subsurface ocean). Let $z = D$ correspond to the base of the ice shell – the top of the ocean (z positive downward). Boundary conditions are that the water pressure equals $\rho g D$ at $z = D$ (base of the slot) and zero at $z = h$ (instantaneous height of water). In the following, P is the deviation of water pressure from this hydrostatic case ($P = 0$ at $z = D$; $P = \rho g h$ at $z = h$).

For turbulent flow,

$$V = a_1 \sqrt{\left| \frac{\partial P}{\partial z} \right|} , \tag{A18}$$

where the sign of a_1 is opposite that of $\partial P/\partial z$. We assume $\partial W/\partial z = 0$, although flexure of the ice prism is expected [17, 55]. From $\partial Q/\partial z = -\partial W/\partial t$

$$W \frac{\partial V}{\partial z} = -\frac{\partial W}{\partial t} ; \quad \frac{\partial V}{\partial z} = -\frac{1}{W} \frac{\partial W}{\partial t} \tag{A19}$$

$$V = -a_2 z + c_1 ; \quad a_2 = \frac{1}{W} \frac{\partial W}{\partial t} \tag{A20}$$

(a_2 and c_1 are functions of t). Merging (A18) and (A20),

$$\sqrt{\left|\frac{\partial P}{\partial z}\right|} = -\frac{a_2}{a_1}z + \frac{c_1}{a_1} \tag{A21}$$

$$\left|\frac{\partial P}{\partial z}\right| = \left(\frac{a_2}{a_1}\right)^2 z^2 - 2\frac{a_2}{a_1}\frac{c_1}{a_1}z + \left(\frac{c_1}{a_1}\right)^2 \tag{A22}$$

Our boundary conditions are on P, but to integrate (A22) for P we must know where $\partial P/\partial z$ changes sign. This occurs at $z = c_1/a_2$. For convenience, consider the case where $\partial P/\partial z > 0$ for $z < c_1/a_2$ (flow near surface is directed upward, in the negative direction; $a_1 < 0$). Then for $z < c_1/a_2$

$$P = \left(\frac{a_2}{a_1}\right)^2 \frac{z^3}{3} - \frac{a_2}{a_1}\frac{c_1}{a_1}z^2 + \left(\frac{c_1}{a_1}\right)^2 z + c_2 \tag{A23}$$

Applying the constraint $P = \rho g h$ at $z = h$,

$$c_2 = \rho g h - \left(\frac{a_2}{a_1}\right)^2 \frac{h^3}{3} + \frac{a_2}{a_1}\frac{c_1}{a_1}h^2 - \left(\frac{c_1}{a_1}\right)^2 h \ , \tag{A24}$$

so for $z \le c_1/a_2$

$$P = \left(\frac{a_2}{a_1}\right)^2 \left(\frac{z^3 - h^3}{3}\right) - \left(\frac{a_2}{a_1}\right)\left(\frac{c_1}{a_1}\right)(z^2 - h^2) + \left(\frac{c_1}{a_1}\right)^2 (z - h) + \rho g h \ . \tag{A25}$$

For $z > c_1/a_2$, multiply the right side of (A22) by -1 and integrate to obtain

$$P = -\left(\frac{a_2}{a_1}\right)^2 \frac{z^3}{3} + \frac{a_2}{a_1}\frac{c_1}{a_1}z^2 - \left(\frac{c_1}{a_1}\right)^2 z + c_2' \ . \tag{A26}$$

366 The constant can be determined by matching the expressions for P in (A25) and (A26)

367 at $z = c_1/a_2$.

   Case 1: For $a_2 = 0$ ($\partial W/\partial t = 0$), and assuming $c_1 > 0$, $D < c_1/a_2$ and the water is flowing up everywhere. Applying $P = 0$ at $z = D$ yields

$$\left(\frac{c_1}{a_1}\right)^2 = \frac{\rho g h}{D - h} \ . \tag{A27}$$

$h > 0$ means the water table is lowered, consistent with upward flow and $c_1^2 > 0$. From

(A22), (A27) implies a uniform pressure gradient within the water column. For general a_2

but still $D < c_1/a_2$, one can again use (A25), a quadratic equation for c_1/a_1 that provides

both the pressure gradient at the inlet from (A22) and the pressure for elasticity purposes

from (A25).

Case 2: For $h = 0$, applying $P = 0$ at $z = D$ in (A25) yields a quadratic equation

for c_1/a_1 with two imaginary roots. This is symptomatic of the fact that $\partial P/\partial z$ has

become negative for $z < D$, requiring the use of (A26). Matching pressures with (A25)

at $z = c_1/a_2$ yields

$$c_2' = \frac{2}{3}\left(\frac{a_2}{a_1}\right)^2\left(\frac{c_1}{a_2}\right)^3 - 2\left(\frac{a_2}{a_1}\right)\left(\frac{c_1}{a_1}\right)\left(\frac{c_1}{a_2}\right)^2 + \left(\frac{c_1}{a_1}\right)^2\left(\frac{c_1}{a_2}\right) + \rho g h \ . \tag{A28}$$

Inserting this back into (A26) and applying $P = 0$ at $z = D$ yields a cubic equation for

the remaining unknown c_1:

$$0 = -\frac{1}{3}\left(\frac{a_2}{a_1}\right)^2\left[D^3 - 2\left(\frac{c_1}{a_2}\right)^3\right] + \left(\frac{a_2}{a_1}\right)\left(\frac{c_1}{a_1}\right)\left[D^2 - 2\left(\frac{c_1}{a_2}\right)^2\right] - \left(\frac{c_1}{a_1}\right)^2\left[D - \left(\frac{c_1}{a_2}\right)\right] + \rho g h \ .$$
$$\tag{A29}$$

For representative values of a_1 and a_2 near the peak of the cycle in slot velocity (-0.3882

and 2×10^{-5} s^{-1}, respectively), we find that the pressure gradient does diverge from a linear

pressure gradient (as anticipated from A23-A28). Pressure gradients are larger near the

slot inlet than far from the slot inlet. Because dissipation scales as $(\partial P/\partial z)^{3/2}$, this implies

that the averaged dissipation used in this paper (from A.8 and the linear-pressure-gradient

approximation), when compared to the true dissipation, is a mild underestimate.

Author contributions

E.S.K. conceived research. E.S.K. and A.M.R. designed research. A.M.R. wrote the boundary element code. E.S.K. carried out research. Both authors contributed extensively to paper-drafting and redrafting, to the revisions and concomitant additional work, and to the interpretation of the results.

References

1. Hurford, T. A., et al. (2009), Geological implications of a physical libration on Enceladus, *Icarus*, *203*, 541-552.

2. Nimmo, F., et al. (2007), Shear heating as the origin of the plumes and heat flux on Enceladus, *Nature*, *447*, 288-291.

3. Smith-Konter, B.; Pappalardo, R. T. (2008), Tidally driven stress accumulation and shear failure of Enceladus's tiger stripes, *Icarus*, *198*, 435-451.

4. Wahr, J., et al. (2009), Modeling stresses on satellites due to nonsynchronous rotation and orbital eccentricity using gravitational potential theory, *Icarus*, *200*, 188-206.

5. McKinnon, W.B. (2015), Effect of Enceladus' rapid synchronous spin on interpretation of Cassini gravity, *Geophys. Res. Lett.*, *42*, 2137-2143.

6. Iess, L., et al. (2014), The gravity field and interior structure of Enceladus, *Science*, *344*, 78-80.

7. Wang, C-Y; Manga, M.; & Hanna, J.C. (2006), Can freezing cause floods on Mars?, *Geophys. Res. Lett.*, *33*, L20202.

8. Nimmo, F. (2004), What is the Young's modulus of ice?, *Conference on Europa's Icy Shell*, abstract #7005.

9. Nimmo, F. and Manga, M. (2009), Geodynamics of Europa's ice shell, in Pappalardo, R.T., McKinnon, W.B., and Khurana, K., eds., *Europa*, University of Arizona Press, p. 382-404.

10. Gudmundsson, A. (2011), Rock fractures in geological processes, Cambridge University Press, 592 pp.

11. Postberg, F., et al. (2009), Sodium salts in E-ring ice grains from an ocean below the surface of Enceladus, *Nature*, *459*, 1098-1101.

12. Postberg, F., et al., (2011), A salt-water reservoir as the source of a compositionally stratified plume on Enceladus, *Nature*, *474*, 620-622.

13. Waite, J. H., Jr., et al. (2009), Liquid water on Enceladus from observations of ammonia and ^{40}Ar in the plume, *Nature*, *460*, 487-490.

14. Hsu, H.-W., et al. (2015), Ongoing hydrothermal activities within Enceladus, *Nature*, *519*, 207-210.

15. Crouch, S.L., & Starfield, A.M. (1983), Boundary element methods in solid mecchanics, George Allen & Unwin.

16. Rubin, A.M., & Pollard, D.P. (1988), Dike-induced faulting in rift zones of Iceland and Afar, *Geology*, *16*, 413-.

17. Reeh, N. (1968), On the calving of ice from floating glaciers and ice shelves, *J. Glaciol.*, *7*, 215-232.

18. Nalluri & Featherstone's Civil Engineering Hydraulics, 5th edition (2009), revised by M. Marriott. Wiley-Blackwell.

19. Tritton, D.J. (1988), Physical Fluid Dynamics, 2nd Edition, Oxford University Press, 544 pp.

20. McKenzie, D., et al. (2000), Characteristics and consequences of flow in the lower crust, *J. Geophys. Res. - Solid Earth*, *105*, 11029-11046.

21. Cuffey, K., & Patterson, W. (2010), The physics of glaciers, 4th edition, Academic Press.

22. Moore, W.B., et al. (2007), The interior of Io, *in* Io after Galileo, edited by Rosaly M.C. Lopes and John C. Spencer, Springer-Praxis Books.

23. Gerya, T. (2010), Introduction to numerical geodynamic modelling, Cambridge University Press.

24. Davis, D., Suppe, J., & Dahlen, F.A. (1983), Mechanics of fold-and-thrust belts and accretionary wedges, *J. Geophys. Res.*, *88*, 1153-1172.

25. Helfenstein, P., et al., (2008), Enceladus South Polar Terrain Geology: New Details From Cassini ISS High

26. Barr, A. C.; Preuss, L. J. (2010), On the origin of south polar folds on Enceladus, *Icarus*, *208*, 499-503.

27. Martens, H., Ingersoll., A.P., Ewald., S.P., Helfenstein, P., & Giese, B. (2015), Spatial distribution of ice blocks on Enceladus and implications for their origin and emplacement, *Icarus*, *245*, 162-176.

28. Schmidt, P., Schmidt, J., & White, O. (2011), The snows of Enceladus, *EPSC-DPS Joint Meeting, Nantes, France*, *451*, 685-688.

29. Howett, C., et al. (2015), Enceladus' enigmatic heat flow, American Astronomical Society, Division for Planetary Sciences meeting #46, abstract number #405.02.

30. Hansen, C. J.; Shemansky, D. E.; Esposito, L. W.; Stewart, A. I. F.; Lewis, B. R.; Colwell, J. E.; Hendrix, A. R.; West, R. A.; Waite, J. H., Jr.; Teolis, B.; Magee, B. A., The composition and structure of the Enceladus plume, *Geophysical Research Letters*, *38*, L11202.

31. Soderlund, K.M., Schmidt, B.E., Wicht, J., & Blankenship, D.D. (2014), Ocean-driven heating of Europa's icy shell at low latitudes, *Nature Geoscience*, *7*, 16-19.

32. Porco, C.; DiNino, D.; Nimmo, F. (2014), How the Jets, Heat and Tidal Stresses Across the South Polar Terrain of Enceladus are Related, *Astronomical J.*, *148*, 45.

33. Spitale, J. N.; Hurford, T. A.; Rhoden, A. R.; Berkson, E. E.; Platts, S. S., Curtain eruptions from Enceladus' South-Polar Terrain, *Nature*, *521*, 57-60.

34. Crawford, G. D.; Stevenson, D. J. (1988), Gas-driven water volcanism in the resurfacing of Europa, *Icarus*, *73*, 66-79.

35. Abramov, O., et al. (2015), Temperatures of vents within Enceladus' tiger stripes, *46th Lunar & Planetary Science Conference*, abstract number 1206.

36. Olgin, J.G., Smith-Konter, B.R., & Pappalardo, R.T. (2011), Limits of Enceladus's ice shell thickness from tidally driven tiger stripe failure, *Geophys. Res. Lett.*, *38*, L02201.

445 37. Nimmo, F., et al. (2014), Tidally modulated eruptions on Enceladus: *Cassini* observations and models,
446 *Astronomical J.*, *148*, 48.
447 38. Běhounková, Marie, et al. (2015), Timing of water plume eruptions on Enceladus explained by interior
448 viscosity structure, *Nature Geoscience*, doi:10.1038/NGEO2475.
449 39. Thomas, P.C., R. Tajeddine, M.S. Tiscareno, J.A. Burns, J. Joseph, T.J. Loredo, P. Helfenstein, C. Porco
450 (2015), Enceladus's measured physical libration requires a global subsurface ocean, *Icarus*, *264*, 37-47.
451 40. Marston, R.A. 1983. Supraglacial stream dynamics on the Juneau Icefield. Annals of the Association of
452 American Geographers 73(4), 597-608.
453 41. Aldridge, B.N., & J.M. Garrett (1973), Roughness coefficients for stream channels in Arizona, US Geological
454 Survey, Open-file report 73-3.
455 42. Brown, M.E., & Hand, K.P. (2013), Salts and radiation products on the surface of Europa, *Astron. J.*, *145*,
456 110.
457 43. Roth, L., et al., (2014), Orbital apocenter is not a sufficient condition for HST/STIS detection of Europa's
458 water vapor aurora, *Proceedings of the National Academy of Sciences*, doi:10.1073/pnas.1416671111.
459 Greenberg, R., 44. Geissler, P., Tufts, B. R., & Hoppa, G. V. (2000), Habitability of Europa's crust: The role of
460 tidal-tectonic processes, *J. Geophys. Res.,* , 105, 17551
461 45. Nimmo, F. and Spencer, J. R. (2013), Enceladus: An Active Ice World in the Saturn System, *Annual Review
462 of Earth and Planetary Sciences*, *41*, 693-717.
463 46. McKinnon, W.B. (2013), The shape of Enceladus as explained by an irregular core: Implications for gravity,
464 libration, and survival of its subsurface ocean, *J. Geophys. Res.*, *118*, 1775-1788.
465 47. Travis, B.J., & Schubert, G. (2015), Keeping Enceladus warm, *Icarus*, *250*, 32-42.
466 48. Hand, K. P.; Khurana, K. K.; Chyba, C. F. (2011), Joule heating of the south polar terrain on Enceladus,
467 *Journal of Geophysical Research*, *116*, E4, E04010.
468 49. Vance, S., et al. (2007), Hydrothermal Systems in Small Ocean Planets, *Astrobiology*, *7*, 987-1005.
469 50. Malamud, U.; Prialnik, D. (2013), Modeling serpentinization: Applied to the early evolution of Enceladus
470 and Mimas, *Icarus*, *225*, 763-774.
471 51. Porco, C., et al. (2006), Cassini Observes the Active South Pole of Enceladus, *Science*, *311*, 1393-1401.
472 52. Meyer, J.; Wisdom, J. (2007), Tidal heating in Enceladus, *Icarus*, *188*, 535-539.
473 53. Charnoz, S., Salmon., J., & Crida., A. (2010), The recent formation of Saturn's moonlets from viscous
474 spreading of the main rings, *Nature*, *465*, 752-754.
475 54. Bland, M.T., et al. (2012), Enceladus' extreme heat flux as revealed by its relaxed craters *Geophys. Res.
476 Lett.*, *39*, L17204.
477 55. Sergienko, O.V. (2010), Elastic response of floating glacier ice to impact of long-period ocean waves, J.
478 Geophys. Res. *115*, F04028,doi:10.1029/2010JF001721, 2010

Notes

1. This can be seen by considering an inviscid fluid column sealed at the bottom and subject instantaneously to a water-pressure gradient of $P_{max}/H(t = 0) \approx P_{max}$ / $0.9Z$. The column adjusts to $H(t = \tau_{adj}) = P_{max}/(\rho_w g)$ where τ_{adj} is an adjustment timescale. Euler's equation of inviscid motion gives $H(t) \sim (P_{max}/\rho_w H)t^2$, so $\tau_{adj} \sim \sqrt{H/g}$. Viscosity does not greatly alter these conclusions for the solutions that match *Cassini* data (Fig. 2). The water table tracks the rising pressure when $\tau_{adj}/p \ll 1$. For $Z \sim 20$ km and $P_{max} = 1$ bar, this ratio of timescales is $O(10^{-3})$ for Enceladus and $O(10^{-4})$ for Europa; negligibly small.
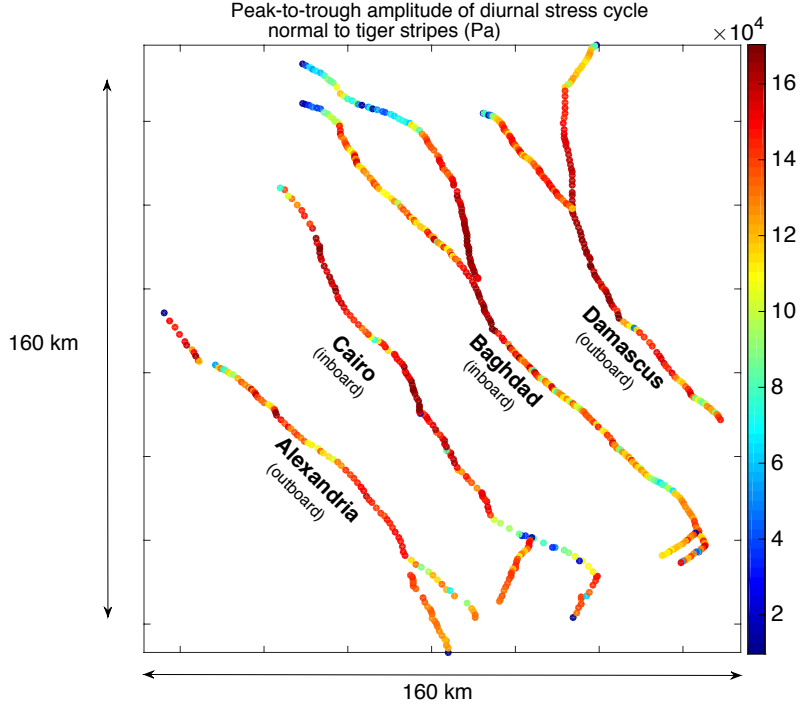
479

Figure S1. Map of the peak-to-trough amplitude of the diurnal cycle in normal stress across Enceladus' tiger stripes for $h_2 = 0.2$, $l_2 = 0.04$. Along-fissure lengths for tiger stripes range (in our mapping) from 133 km (Alexandria *and* Damascus) to 194 km (Cairo), mean 158 km. Great-circle distances between the tips of currently active regions as reported by [32] range from 79 km (Alexandria) to 165 km (Baghdad), mean 122 km. The tiger stripes shown here are the ones that appear freshest and most prominent in imagery of the surface. There is generally good correlation between topographically-prominent tiger stripes and eruption sources, although [33] show that eruptions also emanate from a branch of Baghdad Sulcus that is not particularly geologically prominent (and so is missing from our map).
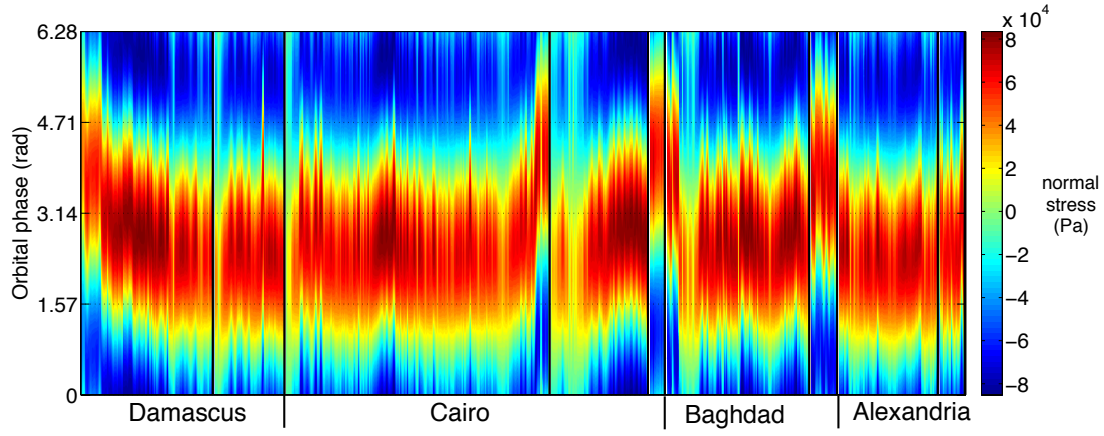
Figure S2. Contour plot of tiger stripe normal stresses as a function of phase and relative distance along the tiger stripes for $h_2 = 0.2$, $l_2 = 0.04$. Each vertical line corresponds to a single vertex picked on the tiger stripes.
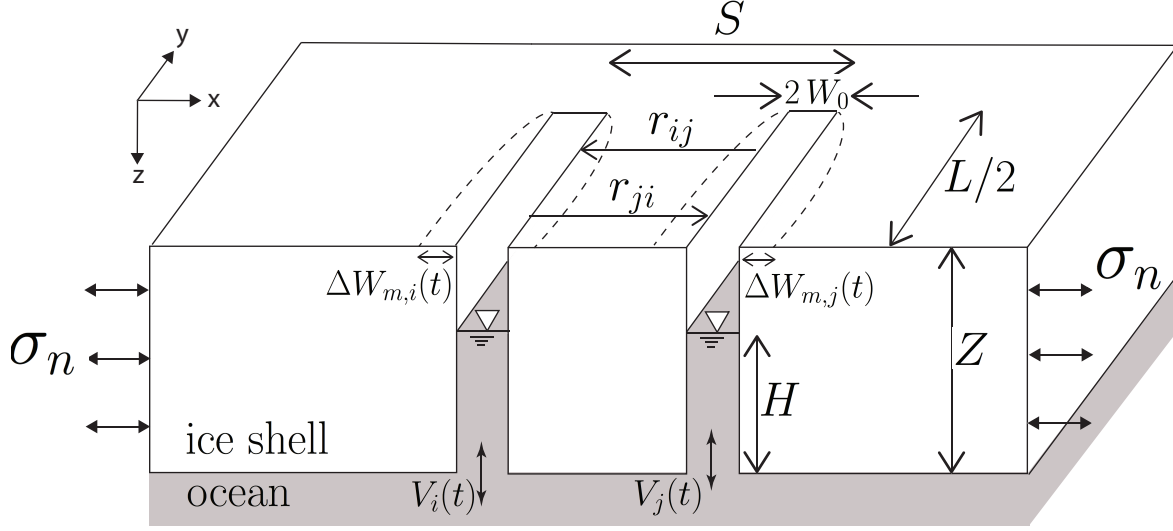
Figure S3. Definitions of terms used in model description (§A.2 - §A.3). Two parallel rectangular slots of uniform stress-free half-width W_0, length L, and spacing S, subject to tidal stress $\sigma_n(t)$, interact elastically (coefficients r_{ij} and r_{ji}). The combination of tidal stress and slot-slot interactions leads to cycles in maximum width change $\Delta W_m(t)$. Cycles in water table height are small relative to zero-stress water table height H. $\Delta W_m(t)$ is coupled to water ingestion/flushing at velocity $V(t)$.

a)

b)

c)

d)

e)
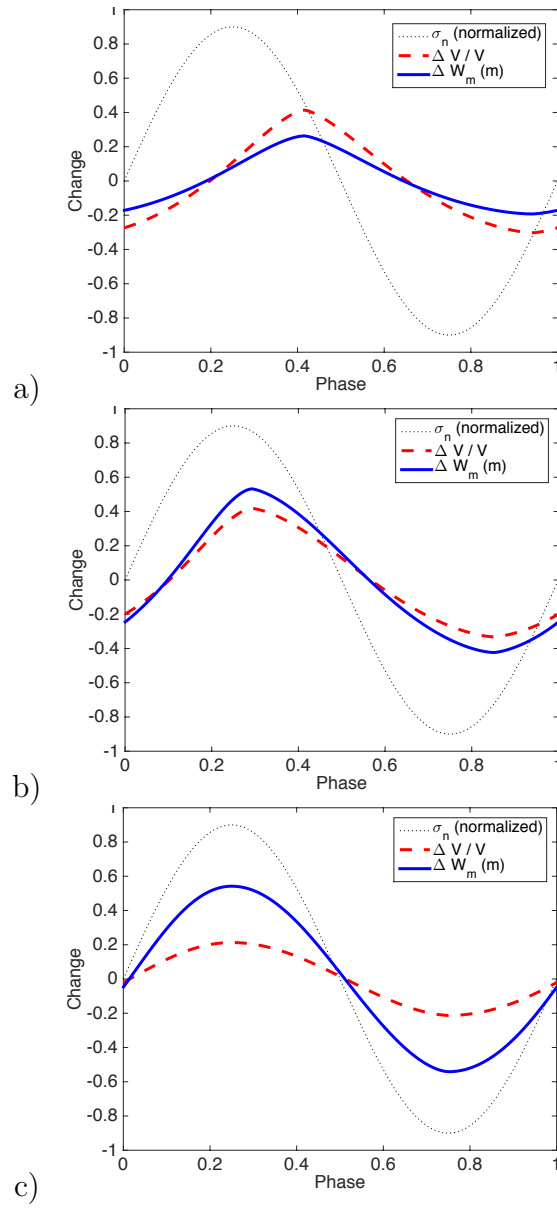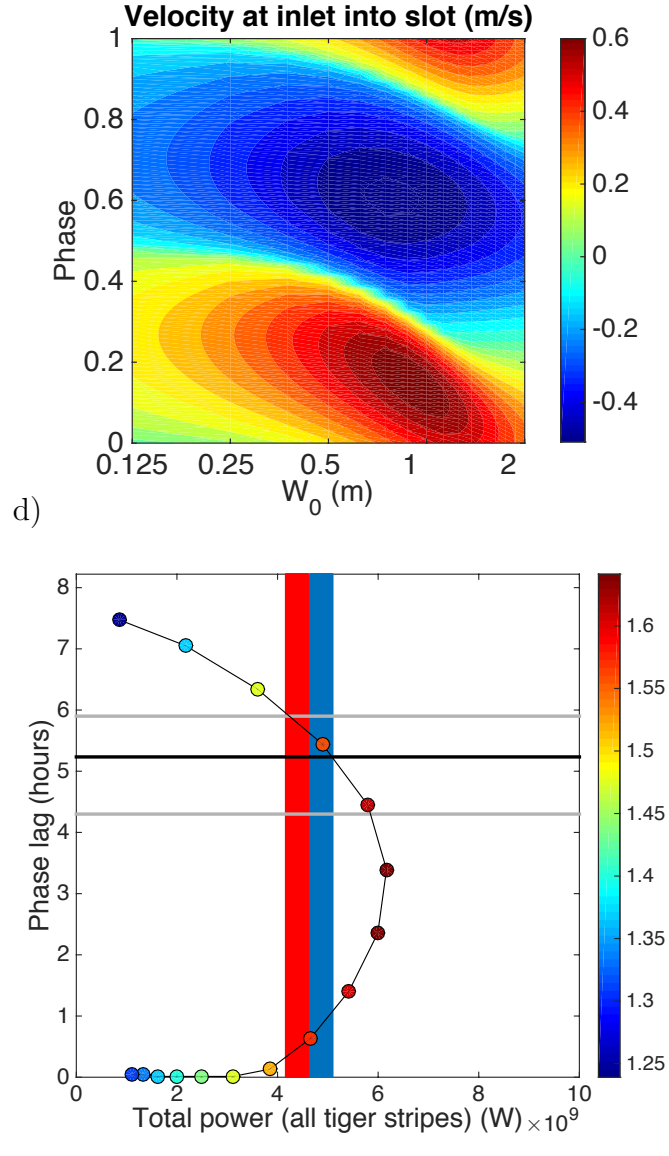
Figure S4.   Tidal flexing cycle for slots that do not interact elastically (for 4 slots each with $L = 100$ km, $E = 6$ GPa). **(a)** Slot half-width $W_0 = 0.5$ m. ΔW_m is maximum width change, $\Delta V/V$ is fractional change in slot water volume, and σ_n is extensional stress normalized to 90% of its own peak amplitude. **(b)** As (a), but $W_0 = 1.0$ m. **(c)** As (a), but $W_0 = 2.0$ m. **(d)** Diurnal cycle of velocity into slot at ocean inlet, as a function of initial width. Contour interval 0.05 m/s. **(e)** Phase lag versus total power output. Initial (tidal-stress-free) half-width is sampled at 0.25 m (uppermost dots) and then at 0.125 m intervals up to 2.5 m (lowermost dots). Dot color corresponds to the fractional change in aperture (max/min) during the tidal cycle. Thick black horizontal line shows phase lag relative to a fiducial model, gray lines show 1σ error in observed phase lag. Red bar shows the observed power output of Enceladus; blue bar includes the additional power inferred for reheating of cold ice at depth.

a)

b)

c)

d)

e)
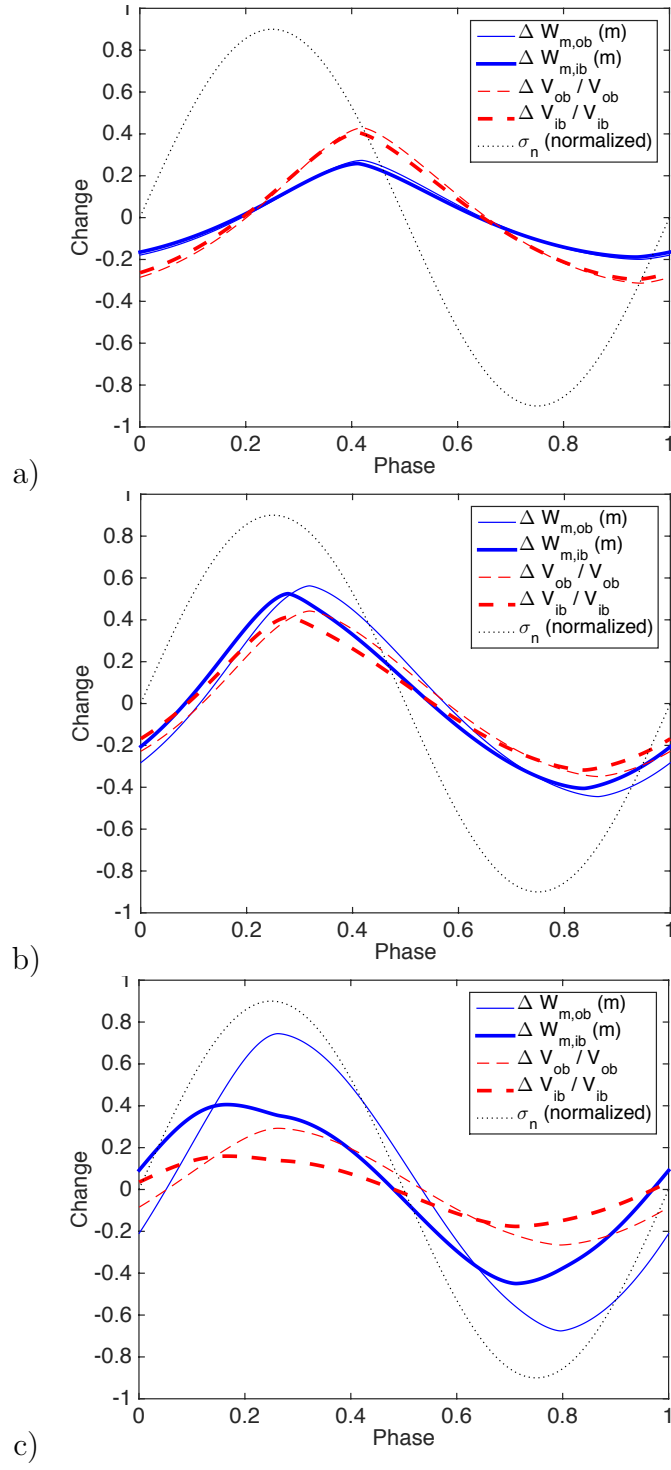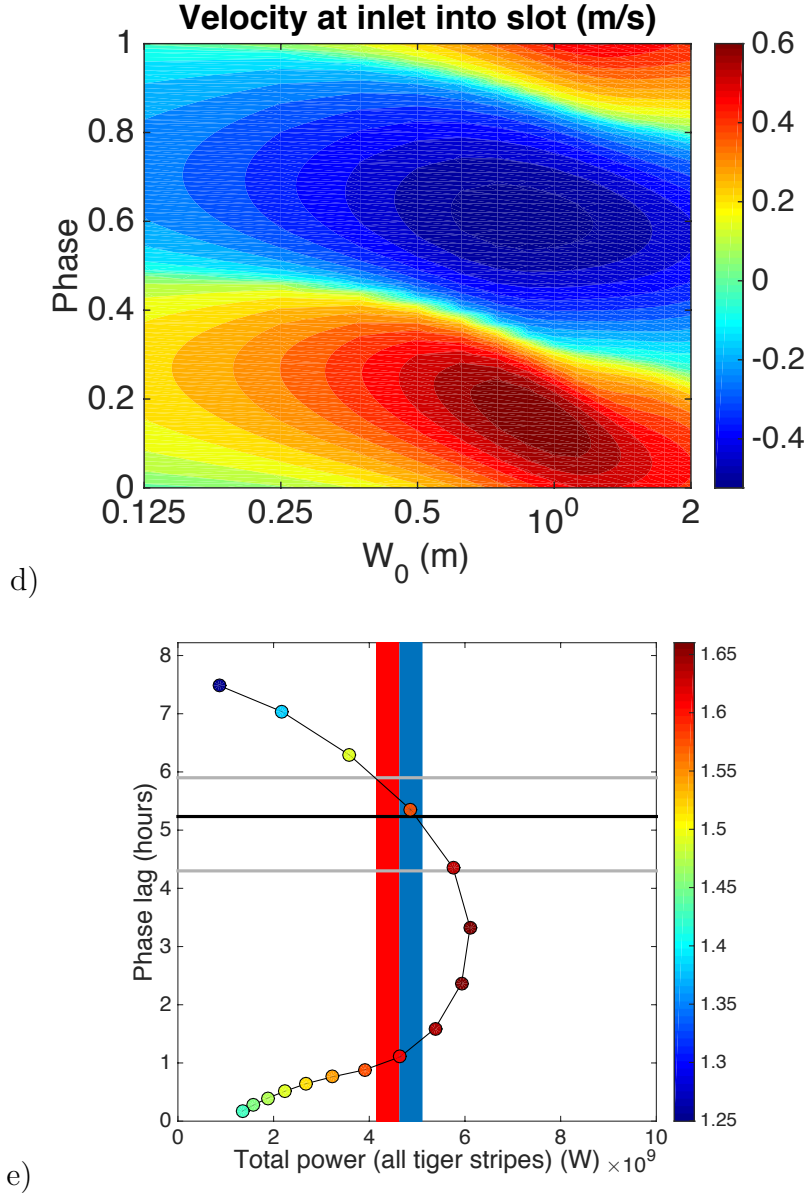
Figure S5.   Tidal flexing cycle for interacting slots assuming 2 inboard (*ib*) and 2 outboard (*ob*) slots, $E = 6$ GPa, $L = 100$ km. **(a)** Slot half-width $W_0 = 0.5$ m. ΔW_m is maximum width change, $\Delta V/V$ is fractional change in slot water volume, and σ_n is extensional stress to 90% of its own peak amplitude. **(b)** As (a), but $W_0 = 1.0$ m. **(c)** As (a), but $W_0 = 2.0$ m. Although outboard-slot deformation leads σ_n, overall power still lags σ_n because most power is generated in the inboard slots. **(d)** Diurnal cycle of velocity into slot at ocean inlet, as a function of initial width. Contour interval 0.05 m/s. Contour interval 0.05 m/s. **(e)** Overall phase lag versus overall power output. Initial (tidal-stress-free) half-width is sampled at 0.25 m (uppermost dots) and then at 0.125 m intervals up to 2.5 m (lowermost dots). Dot color corresponds to the fractional change in aperture (max/min) during the tidal cycle. Thick black horizontal line shows phase lag relative to a fiducial model, gray lines show 1σ error in observed phase lag. Red bar shows the observed power output of Enceladus; blue bar includes the additional power inferred for reheating of cold ice at depth.
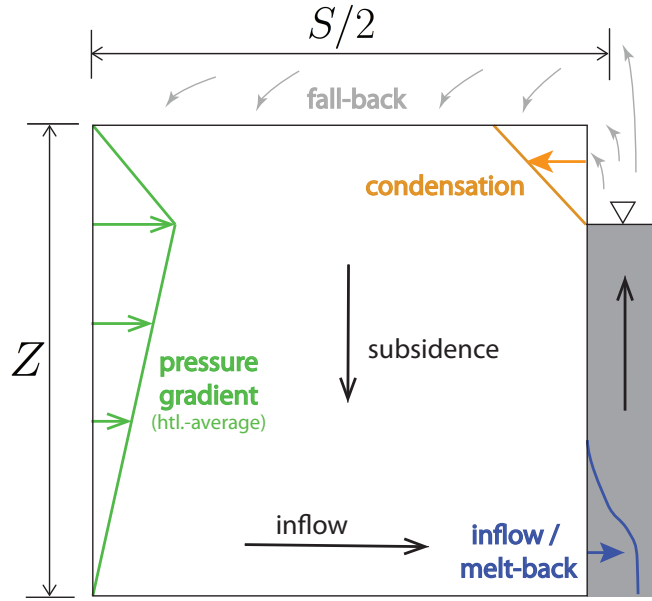
Figure S6.   Long-lived liquid-water slots (that are in isostatic balance with adjacent ice) set up differential stresses (green arrows show vertical gradient in horizontally-averaged differential stress) that drive flow in the adjacent ice shell. Removal of ice by inflow and slot melt-back is compensated by subsidence. Subsidence provides accommodation space for condensation of vapor and for ballistic fall-back of erupted ice particles (materials that would otherwise seal the slot, powering down the eruptions).
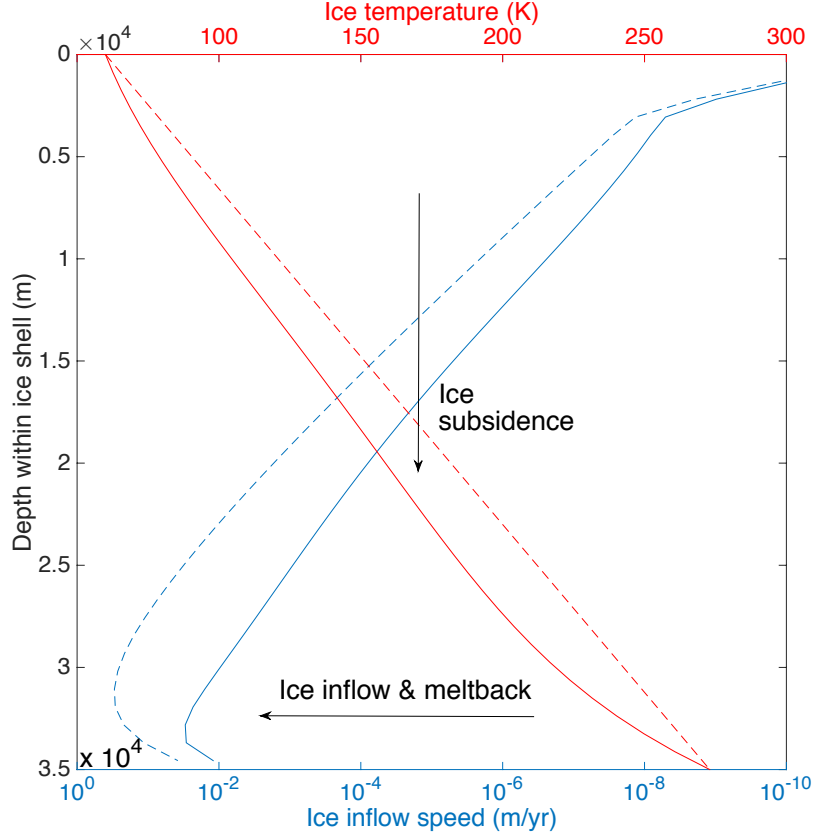
Figure S7. Diagram to show how long-lived water-filled slots affect ice shell tectonics. For an initially-conductive thermal profile within the shell (dashed red line), ice will flow viscously into the slot (dashed blue line), driven by the stress difference between the shell and the slot (Fig. S6). The removal of material from near the base of the ice shell causes subsidence of cold ice from above. This cools the lower shell, in turn reducing inflow. Mean ice inflow is reduced ten-fold at equilibrium (solid lines). Shear tractions τ_{xz} within the ice shell are neglected. Flow is approximated as vertical except in a narrow channel of lateral flow near the base of the shell, which is reasonable because of the large homologous-temperature contrast from the top to the bottom of the shell (~ 0.7) and the strong temperature dependence of the viscosity of ice.
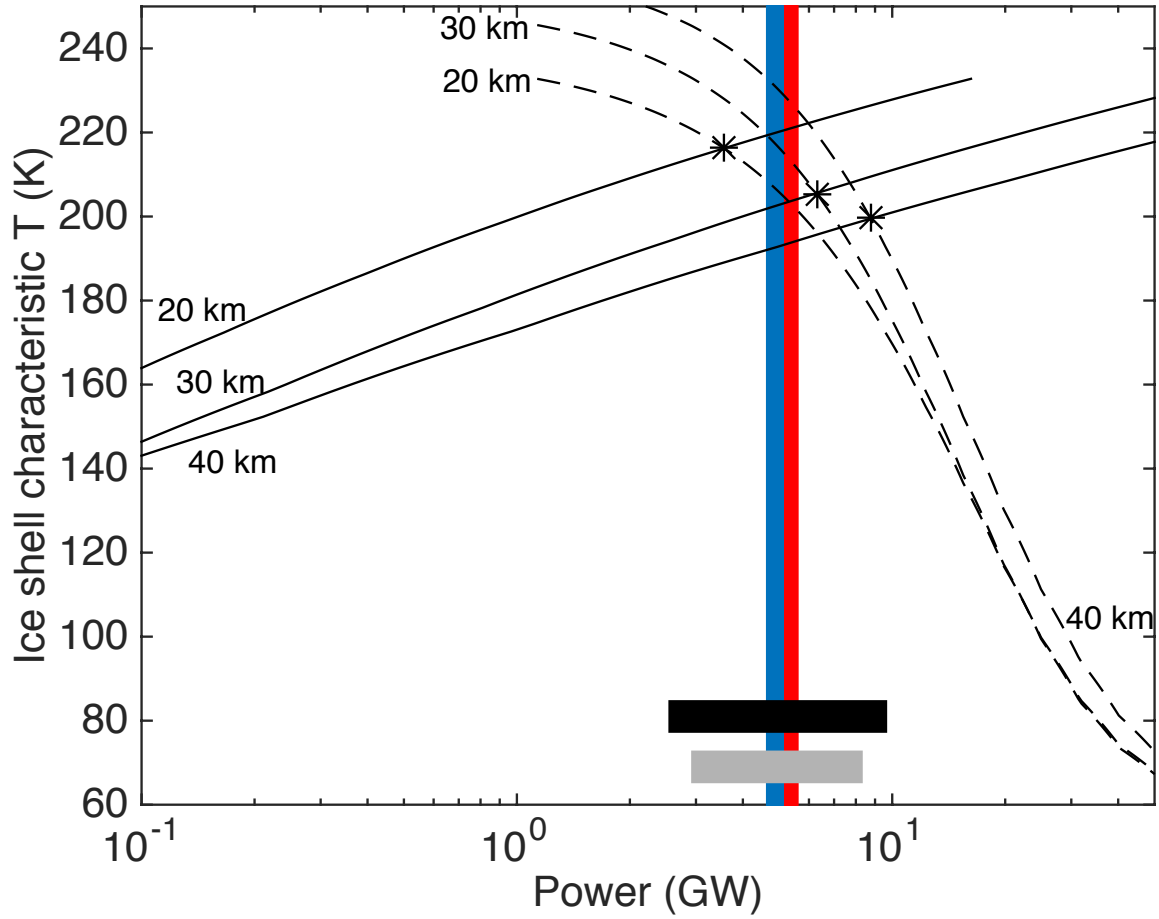
Figure S8. The power output and mass flux of Enceladus, linking 10^{-2} yr through 10^6 yr timescales. Solid black lines show the power corresponding to melting and subsequent vaporization of the ice flowing from the ice shell into base of the slots for ice shell thicknesses of (from top) 20 km, 30 km, and 40 km (the range matching gravity data;[6]), from our ice flow model. Dashed lines show the cooling of the ice shell corresponding to subsidence of cold ice at that mass flux; where the dashed lines intersect the solid lines, shell equilibrium is possible on Myr timescales (black stars). Line terminations correspond to the ends of our model-output look-up table, not to any physical effect. The ordinate corresponds to ice shell characteristic temperature (the temperature at a depth equal to 80% of ice shell thickness). The gray bar shows the power output for the turbulent dissipation models that matches the observed diurnal phase lag (relative to a fiducial model) of Enceladus' eruptions to within 2σ. The black bar shows the range of power output produced by turbulent dissipation model runs that predict a slot aperture that varies by a factor of >1.4, consistent with the observation of large-amplitude diurnal variations in plume flux. The million-year and diurnal-average power outputs implied by long-lived slots agree closely both with each other, and with the observed power output of Enceladus (blue bar; red bar includes the additional power inferred for reheating of cold ice at depth).
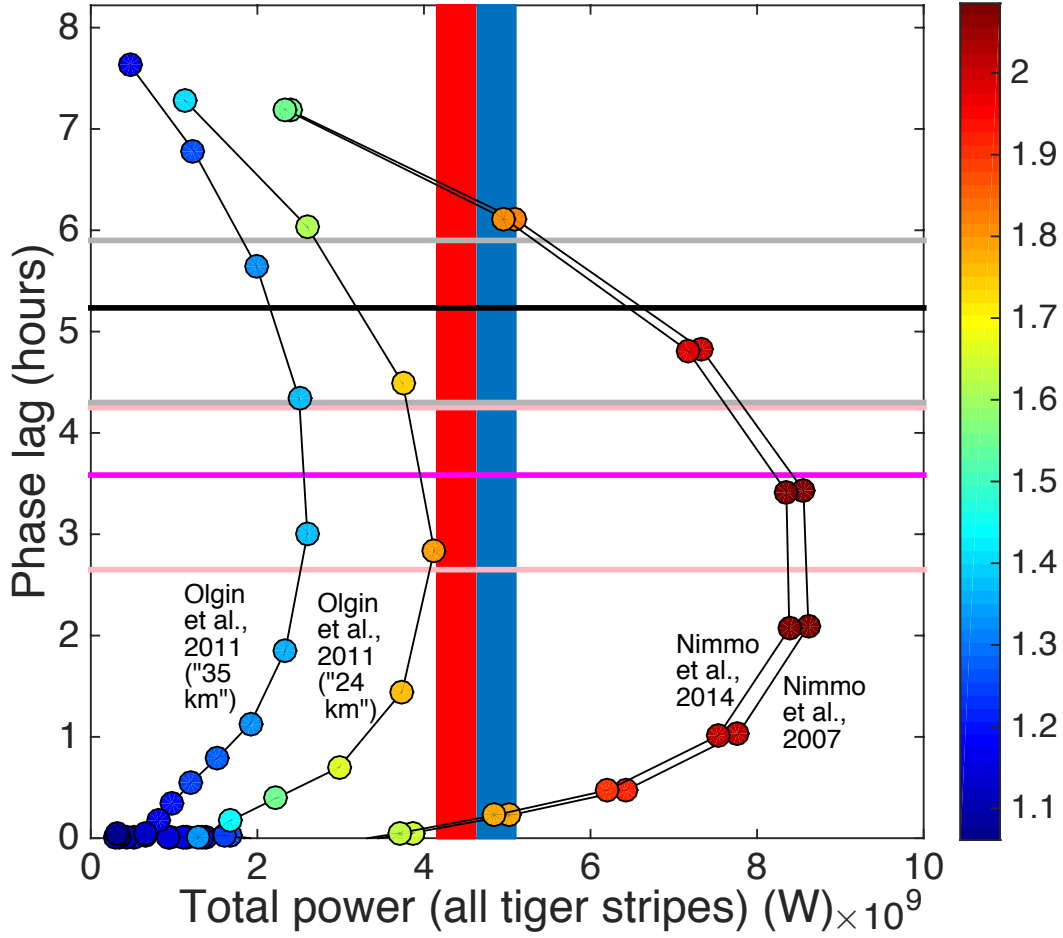
Figure S9.   Sensitivity of time-averaged power to h_2 and l_2, assuming two outboard slots with $L_{ob} = $ 151 km, and two inboard slots with $L_{ib} = 93$ km. [36] use a four-layer Enceladus structure to convert ice shell thickness to h_2 and l_2, whereas [2, 37] use a three-layer Enceladus structure to convert ice shell thickness to h_2 and l_2. The numbers in quotes refer to the global ice-shell thicknesses assumed in calculating h_2 and l_2 (we assume $Z = 24$ km for the Nimmo et al. models). Thick black horizontal line shows phase lag relative to the [2] model, with gray lines showing 1σ error in observed phase lag. Thick magenta horizontal line shows phase lag relative to the [36] model for ice shell thickness of 24 km, with pink lines showing 1σ error in observed phase lag. Dot color corresponds to the fractional change in aperture (max/min) during the tidal cycle. For each curve, initial (tidal-stress-free) half-width is sampled at 0.25 m (uppermost dots) and then at 0.125 m intervals up to 2.5 m (lowermost dots). Red bar shows the observed power output of Enceladus; blue bar includes the additional power inferred for reheating of cold ice at depth.
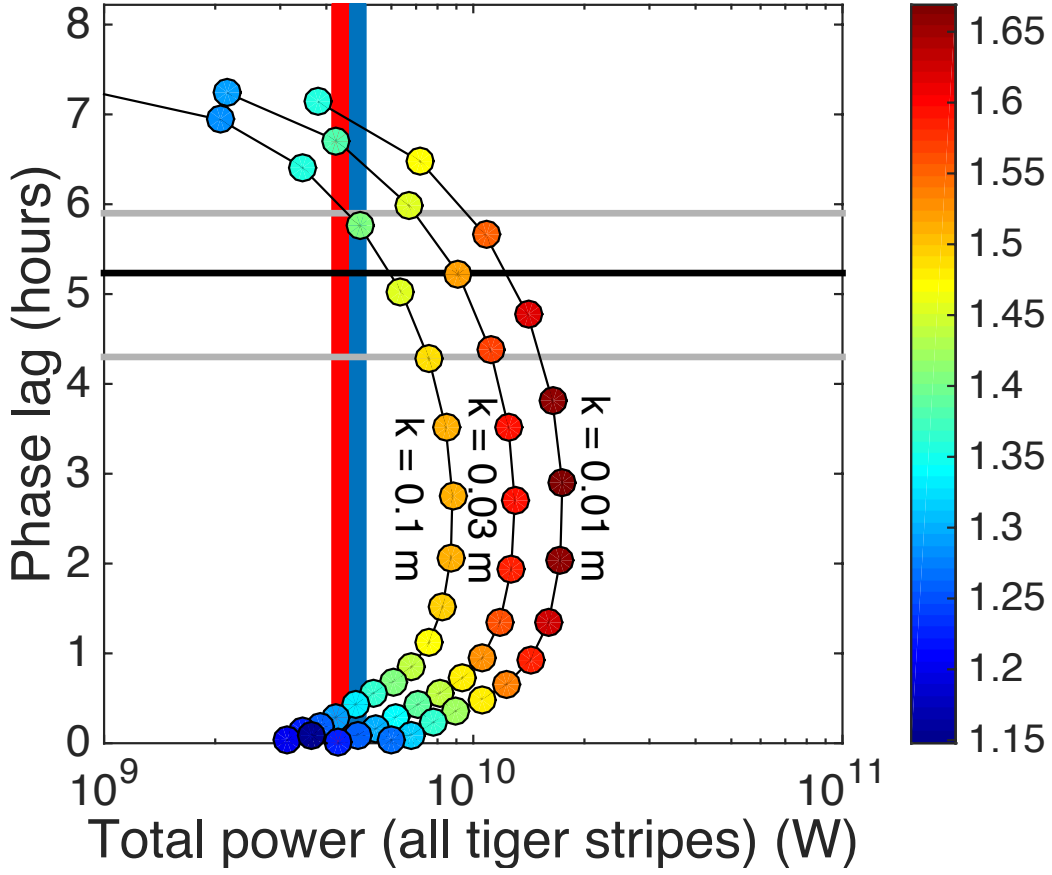
Figure S10.   Sensitivity of power to k (roughness). Assuming two outboard slots with $L_{ob} = 151$ km, and two inboard slots with $L_{ib} = 93$ km. Dot color corresponds to the fractional change in aperture (max/min) during the tidal cycle. For each curve, initial (tidal-stress-free) half-width is sampled at 0.25 m (uppermost dots) and then at 0.125 m intervals up to 2.5 m (lowermost dots). Red bar shows the observed power output of Enceladus; blue bar includes the additional power inferred for reheating of cold ice at depth.
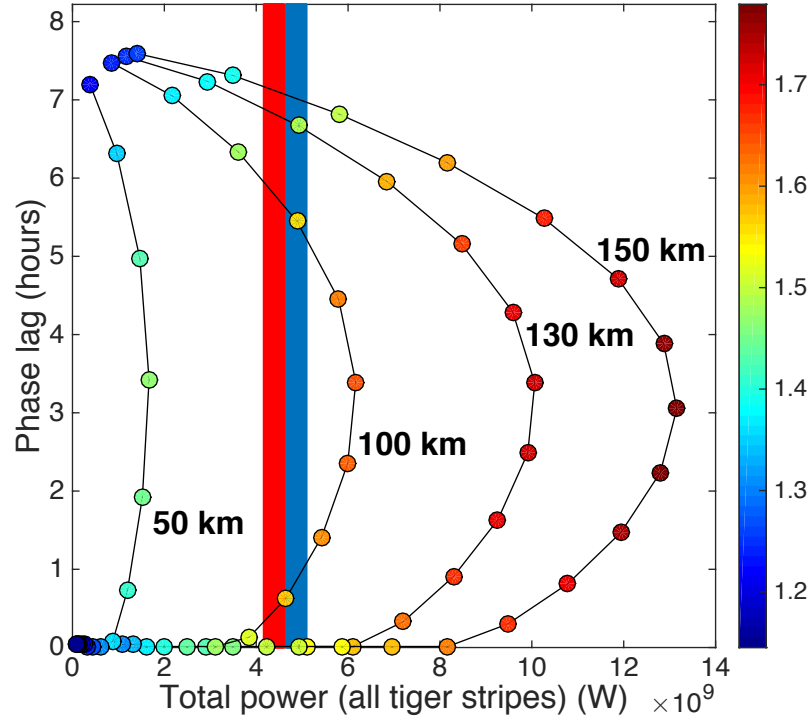
Figure S11. Sensitivity of time-averaged power to L, considering four non-interacting equal-length slots. Dot color corresponds to the fractional change in aperture (max/min) during the tidal cycle. For each curve, initial (tidal-stress-free) half-width is sampled at 0.25 m (uppermost dots) and then at 0.125 m intervals up to 2.5 m (lowermost dots). Red bar shows the observed power output of Enceladus; blue bar includes the additional power inferred for reheating of cold ice at depth.